Development and validation of a 3D anthropomorphic phantom for dental CBCT imaging research

Merken Karen
KU Leuven, Department of Imaging and Pathology, Division of Medical Physics & Quality Assessment, 3000 Leuven, Belgium
karen.merken@uzleuven.be
Corresponding author

Monnens Janne
KU Leuven, Department of Imaging and Pathology, Division of Medical Physics & Quality Assessment, 3000 Leuven, Belgium

Marshall Nicholas
KU Leuven, Department of Imaging and Pathology, Division of Medical Physics & Quality Assessment, 3000 Leuven, Belgium

Nuyts Johan
KU Leuven, Department of Imaging and Pathology, Division of Nuclear Medicine & Molecular Imaging, 3000 Leuven, Belgium

Brasil Danieli Moura
University of Louisville, Department of Diagnosis and Oral Health, School of Dentistry, 40292 Louisville, KY, USA

Santaella Gustavo Machado
University of Louisville, Department of Diagnosis and Oral Health, School of Dentistry, 40292 Louisville, KY, USA

Politis Constantinus
KU Leuven, Department of Imaging and Pathology, Division of Oral and Maxillofacial Surgery, 3000 Leuven, Belgium

Jacobs Reinhilde
KU Leuven, Department of Imaging and Pathology, Division of Oral and Maxillofacial Surgery, 3000 Leuven, Belgium
Karolinska Institute, Department of Dental Medicine, 171 77 Stockholm, Sweden

Bosmans Hilde
KU Leuven, Department of Imaging and Pathology, Division of Medical Physics & Quality Assessment, 3000 Leuven, Belgium

Abstract

Background: Optimization of dental CBCT imaging is still in a preliminary stage and should be addressed using task-based methods. Dedicated models containing relevant clinical tasks for image quality studies have yet to be developed.
Purpose: To present a methodology to develop and validate a virtual adult anthropomorphic voxel phantom for use in task-based image quality optimization studies in dental CBCT imaging research, focusing on root fracture (RF) detection tasks in the presence of metal artefacts.
Methods: The phantom was developed from a CBCT scan with an isotropic voxel size of 0.2 mm, from which the main dental structures, mandible and maxilla were segmented. The missing large anatomical structures, including the spine, skull and remaining soft tissues, were segmented from a lower resolution full skull scan. Anatomical abnormalities were absent in the areas of interest. Fine detailed dental structures, that could not be segmented due to the limited resolution and noise in the clinical data, were modelled using a-priori anatomical knowledge. Model resolution of the teeth was therefore increased to 0.05 mm. Models of RFs as well as dental restorations to create the artefacts, were developed, and could be inserted in the phantom in any desired configuration. Simulated CBCT images of the models were generated using a newly developed multi-resolution simulation framework that incorporated the geometry, beam quality, noise and spatial resolution characteristics of a real dental CBCT scanner. Ray-tracing and Monte Carlo techniques were used to create the projection images, which were reconstructed using the classical FDK algorithm. Validation of the models was assessed by measurements of different tooth lengths, the pulp volume and the mandible, and comparison with reference values. Additionally, the simulated images were used in a reader study in which two oral radiologists had to score the realism level of the model's normal anatomy, as well as the modelled RFs and restorations.
Results: A model of an adult head, as well as models of RFs and different types of dental restorations were created. Anatomical measurements were consistent with ranges reported in literature. For the tooth length measurements, the deviations from the mean reference values were less than 20%. In 77% of all the measurements, the deviations were within 10.1%. The pulp volumes, and mandible measurements were within one standard deviation of the reference values. Regarding the normal anatomy, both readers considered the realism level of the dental structures to be good. Background structures received a lower realism score due to the lack of detailed enough trabecular bone structure, which was expected but not the focus of this study. All modelled RFs were scored at least adequate by at least one of the readers, both in appearance and position. The realism level of the modelled restorations was considered to be good.
Conclusions: A methodology was proposed to develop and validate an anthropomorphic voxel phantom for image quality optimization studies in dental CBCT imaging, with a main focus on root fracture detection tasks. The methodology can be extended further to create more models representative of the clinical population.

Keywords: virtual phantom modelling, dental pathoses and restorations, CBCT imaging, medical imaging simulations, clinical task-based optimization

I. INTRODUCTION

Over the past two decades, cone beam computed tomography (CBCT) imaging has become an extensively used tool for diagnosis and treatment planning in oral healthcare[1]. Currently, more than 200 CBCT models produced by 47 manufacturers are available on the world market, operating under a broad range of imaging protocols, leading to system performance that varies widely in terms of both radiation exposure and clinical diagnostic performance[1–6]. This suggests that optimization of dental CBCT imaging is still in a very early stage and needs to be addressed.

Optimization aims to find the appropriate balance between image quality and patient radiation dose for a specific clinical task. Clinical trials[7,8] have been considered the gold standard for system evaluation and optimization. However, in practice, these studies face several difficulties due to ethical limitations, costs, time limitations, case selection (especially for less common pathoses), or a fundamental lack of ground truth, i.e., the knowledge of the patient's exact anatomy and pathological condition. Nowadays, virtual imaging trials (VITs)[7,8] are becoming a powerful alternative to clinical trials. As illustrated in Figure 1, in a complete VIT, the patient, the imaging system, and the image interpretation are replaced by computational models. A VIT can avoid many of the challenges of a

clinical trial, and enables system performance evaluation in a controlled environment where the ground truth is exactly known. Additionally, VITs have the potential to evaluate new technologies prior to use in clinical practice. However, they are not free from difficulties. The imaging system must be accurately modelled, patient model anatomy and pathological condition should be sufficiently realistic, and the virtual observer should be able to mimic or substitute interpretation by the radiologist.

One of the crucial steps in setting-up a VIT platform is the development of computational patient models, representative of the clinical population under study, containing clinically interesting tasks. Virtual anthropomorphic phantoms have been previously developed for various applications in medical imaging[9–19]. For dental CBCT imaging in particular, several phantoms are available for dosimetry applications[10,12–16,18]. Nevertheless, for image quality studies, the available models do not suffice for various reasons: lack of detailed dental and cranio-maxillofacial structures, the absence of clinically interesting tasks, and in case of voxel phantoms, often insufficient spatial resolution of the model.
For image quality studies, an important aspect of developing computational phantoms is the modelling of clinical tasks that are relevant and challenging. There are numerous dental pathoses, and CBCT imaging is indicated in many fields within dentistry including endodontics, periodontics, orthodontics, oral and maxillofacial surgery, and implant planning. One of the most challenging tasks remains the diagnosis of root fractures (RFs)[20–26], and currently, there is still no consensus on the accuracy of CBCT imaging regarding RF detection. Any tooth can be subject to a fracture, however, the main difficulty is that RFs are typically found in endodontically treated teeth. This severely complicates the diagnosis, as most dental restorative materials are very dense causing image artefacts that can mask the RF or generate lines mimicking a RF, leading to a misdiagnosis[21]. Additionally, artefacts caused by dental restorations in neighbouring teeth can also hamper RF detection in a nearby tooth, which may or may not be endodontically treated. Correct diagnosis of the fracture is crucial as this determines whether the tooth in question will be extracted or not[20]. Early RF diagnosis can also prevent inflammation of surrounding tissues. This is important as inflammation could lead to bone resorption resulting in costly and time consuming therapeutic interventions[27].

Detailed computational anthropomorphic head models containing relevant clinical features for task-based image quality optimization studies in dental CBCT imaging appear to be lacking in the literature. The objective of this work is therefore to present a methodology to develop and validate a prototype adult anthropomorphic head voxel phantom for image quality related studies. RF detection in the presence of metal artefacts is considered the main clinical task of interest. Used in conjunction with the available dosimetry phantoms, optimization studies balancing radiation dose and image quality can be performed. The development of this model is the first step towards the development of more models representative of the clinical population.

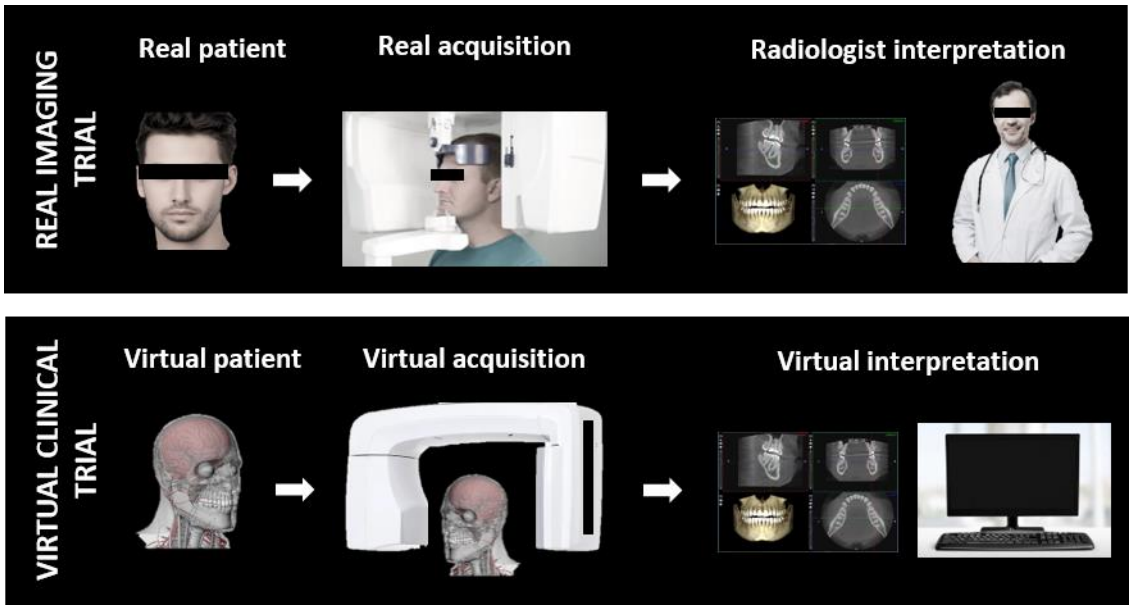

Figure 1. Visualization of a real and virtual imaging trial, illustrated specifically for dental CBCT imaging (adapted from literature[7]).

II. METHODS

a. Anthropomorphic voxel phantom development

Voxel phantom anatomy was based on segmentations from clinical dental CBCT scans of adults, assuring a realistic model of patient anatomy. Data from normal patients were selected. Fine detailed structures, which could not be segmented due to the limited resolution and noise in the clinical data, were modelled. A specific modelling methodology was developed for the teeth as well as the surrounding cranio-maxillofacial structures. Segmentation and modelling was performed using 3D Slicer software[28].

i. Patient selection

Clinical dental CBCT images were selected from the PACS database of the UZ Leuven University Hospital. The use of retrospective patient data was approved by the medical ethics research council of the UZ/KU Leuven. The data was acquired on a NewTom VGi EVO system (Cefla, Italy) which is used for the majority of patient examinations (360° gantry rotation, 110 kVp). Only patients between 20 and 25 years-old were considered, given the relationship between increasing age and the amount of dental restorations present[29]. Only data from normal patients were included, i.e., not showing anatomical abnormalities, missing or supernumerary teeth, pathoses or dental restorations in the areas of interest. Additionally, for this prototype phantom, anatomical dimensions of the teeth[30] and mandible[31] were chosen to be within 20% or one standard deviation from reported population mean values as to approximate a standard patient. Images with the highest possible resolution were also preferred. For this study, eventually image data from two patients were selected.

The teeth, mandible and maxilla were segmented from a medium field of view (FOV) size scan (12x8 cm²) of a 21-year-old female patient (patient A) with an isotropic voxel size of 0.2 mm. The image was taken in preparation for wisdom teeth extraction. None of the above criteria were mentioned in the radiological report or observed in the image. Additionally, the patient had no history of previous significant dental treatments. The image also provided the highest possible resolution while still encompassing most of the important anatomical regions. Higher resolution scans have smaller FOV sizes, only showing parts of these structures. The adjacent missing large anatomical structures, including the cervical vertebrae, skull and remaining soft tissues, were segmented from a full skull scan (24x19 cm² FOV size with 0.3 mm voxel size) of another 21-year-old female patient (patient B). For the selection of this patient, the state of the dentition was not important. However, to facilitate the production of a single model, patient B was selected such that the anatomical structures of the two patients matched sufficiently. Therefore, measurements were performed on the scans of both patients; the distance between the mandibular foramens and coronoid processes was the same to within respectively 1.2 mm and 1.8 mm. Additionally, the distance between the zygomatic arches was the same to within 7 mm, and the tilt angle of the airways of both patients was also approximately the same.

ii. Tooth modelling

For the modelling of the teeth, first a volume of interest (VOI) was cropped around each tooth in the CBCT volume of patient A. The cropping was followed by applying gradient anisotropic diffusion[32] to reduce image noise while preserving edges. Next, linear isotropic interpolation was used to upsample the spatial resolution of the tooth models from 0.2 mm to 0.05 mm. This allowed the addition of fine dental structures to the model. An upsampling factor of four was chosen to provide a good trade-off between model accuracy and model size. Figure 2a illustrates the described preprocessing steps for tooth modelling.

The main dental structures (enamel, dentin, and pulp) were segmented from the preprocessed VOIs following the procedure illustrated in Figure 2b. First, a grow-cut based algorithm[33] was applied to obtain a rough segmentation of the whole tooth which was further refined using a median filter for surface smoothing. In all of the following modelling steps, surface smoothing of the segments was performed using median filtering. The filter kernel size was set experimentally based on the roughness and size of the structure. The segmentation algorithm required as input manually drawn seeds in the final structure as well as the surrounding background. Next, within the resulting tooth segment, the segmentation method was reapplied to extract the combined dentin and pulp segment. Local smoothing was manually performed on the border between the enamel and the dentin. The pulp was also segmented using the grow-cut based method and smoothed afterwards. Segmentations were then logically subtracted to obtain the final segments; subtraction of the combined dentin and pulp segment from the tooth

segment gave the enamel. Dentin was isolated by subtracting the pulp segment from the combined dentin and pulp segment.

Due to the limited resolution and noise in the clinical data, direct segmentation of small structures, i.e., the periodontal ligament space (PLS), the lamina dura (LD), and the pulp located in the apical part of the root, was not possible. These structures were therefore modelled using a-priori anatomical knowledge.

The PLS, a thin layer of connective tissue of thickness 0.15-0.21 mm[34] surrounding the root of the tooth, was modelled using the hollow function[33]. This function replaces a segment by a user specified uniform-thickness shell defined by the segment boundary[33]. It was applied to the combined dentin and pulp segment. The LD, a layer of cortical bone adjacent to the PLS, was modelled in the same manner. Its thickness varies between 0.22 and 0.54 mm[35]. Shell thicknesses of 0.15 and 0.4 mm were chosen for the PLS and the LD respectively. Logical operators were used to ensure the PLS and the LD did not extend across the mandible and maxilla.

The missing apical part of the pulp was modelled by delineating circles of decreasing size in every other two slices starting from the most apical segmented pulp to the root apex. Shape-based interpolation was used to complete the segmentation. The smallest diameter of the pulp, taken at 1 mm short of the root apex, varies between 0.14 and 0.34mm[36]. Smoothing of the whole pulp segment was not straightforward due to its small dimensions, mainly the apical part. Therefore, the size of the pulp segment was first increased by a specified margin. The segment was then smoothed, and its size was shrunk again using the same margin.

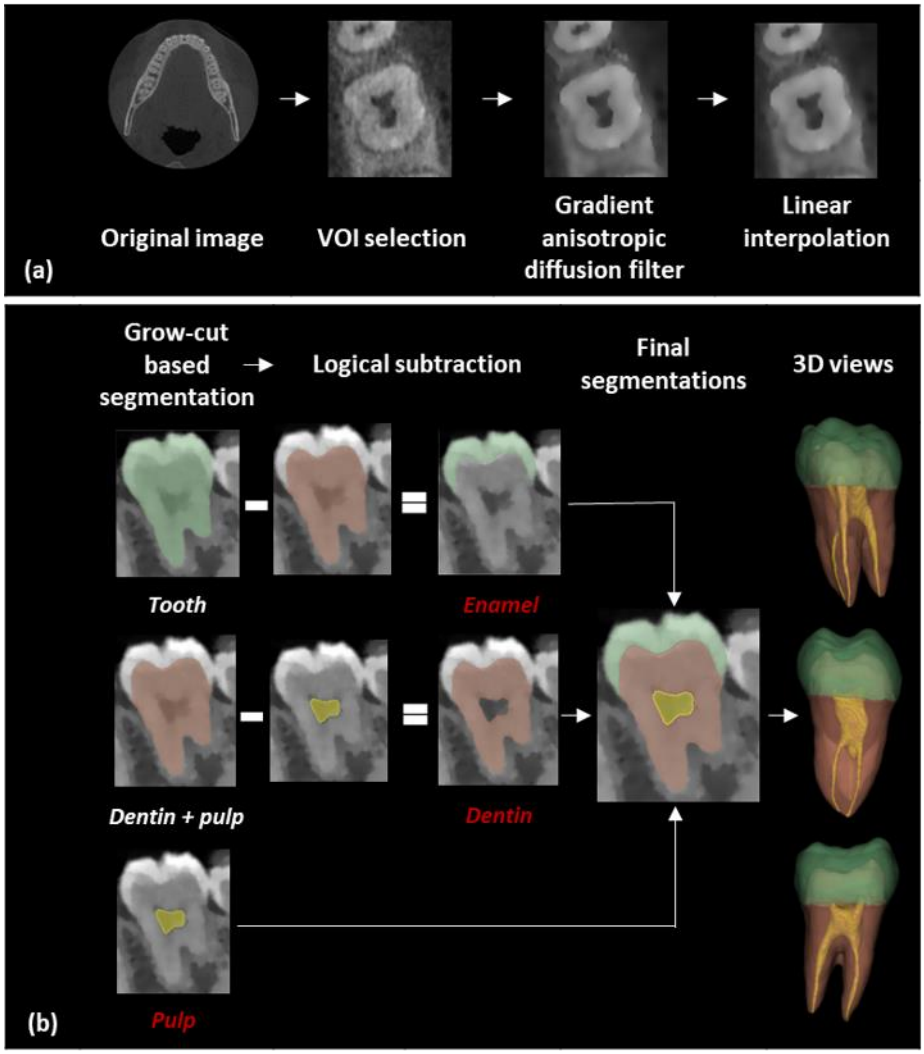

Figure 2. (a) Illustration of the image pre-processing steps for tooth modelling, and (b) the segmentation procedure to obtain the main dental structures: enamel, dentin, and pulp. The enamel segment is shown in green, the dentin segment in brown, and the pulp segment in yellow. Only one image view is shown.

iii. Cranio-maxillofacial modelling

The cranio-maxillofacial structures, i.e., the bone structures, the mandibular and maxillary canals, the surrounding soft tissues, as well as the air holes, were segmented from both patient scans. Given the size of these structures, direct segmentation from the scans was possible, except for the smaller trabeculae of the trabecular bone structure which could not be segmented. Clinical image data from patients showing the trabecular bone structure in full detail as well as the complete mandible and maxilla are not available. An alternative could be to model the trabecular bone mathematically using the incomplete segmentation as a starting point. However, this was not pursued as the focus of this work was on modelling tooth pathoses. The spatial resolution of the cranio-maxillofacial structures was therefore set to 0.2 mm to keep the computational load of the model in simulations reasonably low while still providing sufficient resolution for the remaining cranio-maxillofacial structures. This led to the development of a multi-resolution phantom.

Preprocessing was again applied before segmentation. First, the CBCT scan of patient B was cropped to obtain the structures that patient A was missing. Then, on both image volumes, gradient anisotropic diffusion was performed. Linear isotropic interpolation was then applied to the data of patient B to increase the resolution from 0.3 mm to the set resolution of 0.2 mm.
A separate segmentation procedure was followed for each of the different types of structures. The following bone structures were segmented: the maxilla, mandible, zygomatic and hyoid bone from patient A, and the cervical vertebrae, the sphenoid, temporal, parietal, and occipital bones from patient B. Bone structures consist of cortical and trabecular bone. Cortical bone is a dense tissue, while trabecular bone is a honeycomb-like trabecular network containing dense trabeculae surrounded by soft tissue components. First, a mask of all the bone structures, cortical and trabecular bone combined, was created. A rough segmentation of the dense cortical bone and the dense trabeculae was obtained using thresholding. The soft tissue components of the trabecular bone structure were then added to the segment by manually filling the segmented bone structure. Next, smoothing was applied, using median filtering with an experimentally determined kernel size. Within the resulting mask, consecutive local thresholds were then applied to isolate as accurately as possible the soft tissue components of the trabecular bone from the dense trabeculae, forming the final soft tissue bone segment.

The soft tissue bone segment was then logically subtracted from the mask to obtain the final segment of all the dense bone structures. The inferior alveolar canals in the mandible and the incisive canal in the maxilla were segmented via thresholding, followed by manual refinements and local smoothing. The canals were subtracted from the bone structure segments to remove overlap. As different soft tissues are indistinguishable on a CBCT scan, soft tissues had to be segmented as a whole, for which thresholding was used. Only structures outside the mask defined by all the previous defined segments were included. Finally, the remaining air structures, i.e., the sinuses, the airway, and the mouth cavity could be combined into one segment.
To complete the modelling of the cranio-maxillofacial structures, the segmentations of both patients had to be combined. Therefore, an affine transformation was applied to the structures of patient B to best match the position of the structures of both patients. Manual adjustments were then performed for further refinement. A series of logical operators were also applied to ensure that no gaps or overlapping structures were present in the final model. Figure 3 illustrates the workflow.

b. Modelling of clinical tasks

Different types of RFs and dental restorations were developed. A procedure was worked out to insert the resulting models into the anthropomorphic voxel phantom in any desired configuration, to represent the most common challenging clinical situations.

i. Root fractures (RFs)

RF modelling was based on literature information about RF shape, formation, location, and sizes[20–22,27,37]; Figure 4 shows the procedure. RFs were represented by B-spline volumes created using the NURBS-python package[38]. For the in-plane direction a third-degree spline was defined, while a first-degree spline was used for the perpendicular direction. RFs of different shapes were then created by manual adaptation of the control points, according to the shapes of examples of RFs[20–22,27]. RF volumes were exported as an OBJ file and imported into 3D Slicer for voxelization (0.05 mm). RF thickness, typically between 0.07 and 0.28 mm[27,37], could be adapted by growing or

shrinking a margin. Manual translation and rotation of the RF volume was performed to position the RF within a tooth at the desired location. The RF was then logically subtracted from the dentin segment to actually insert the RF into the dentin.

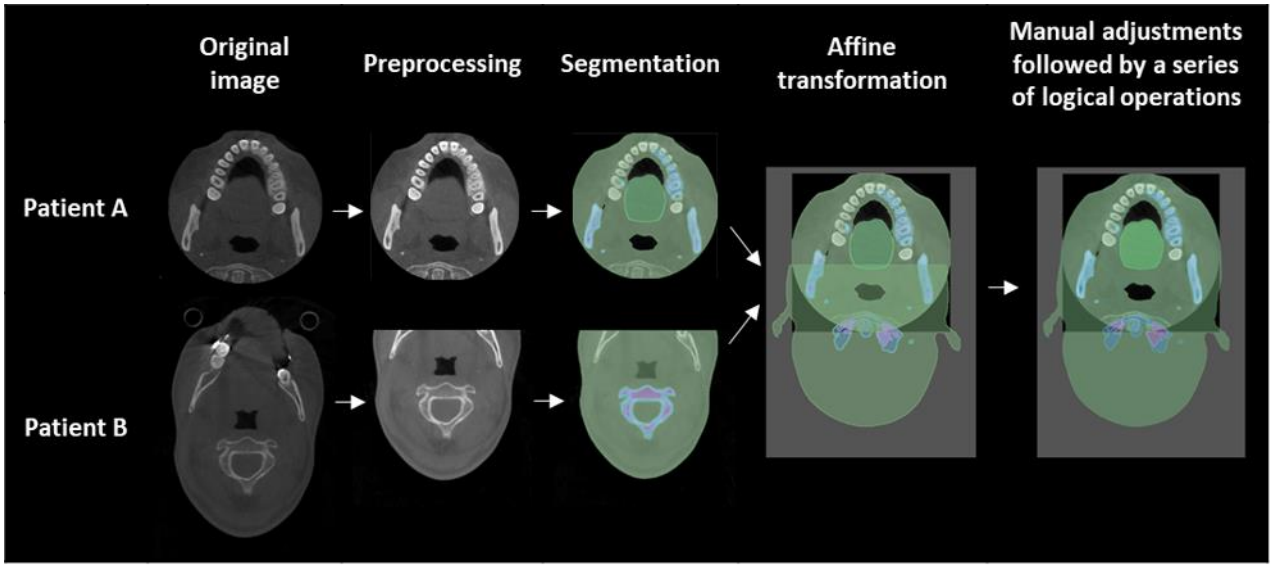

Figure 3. Overview of the developed workflow for modelling the cranio-maxillofacial structures. The soft tissue segment is shown in green, the dense bone segment in blue and the soft tissue bone segment in purple. Only one axial view is shown.

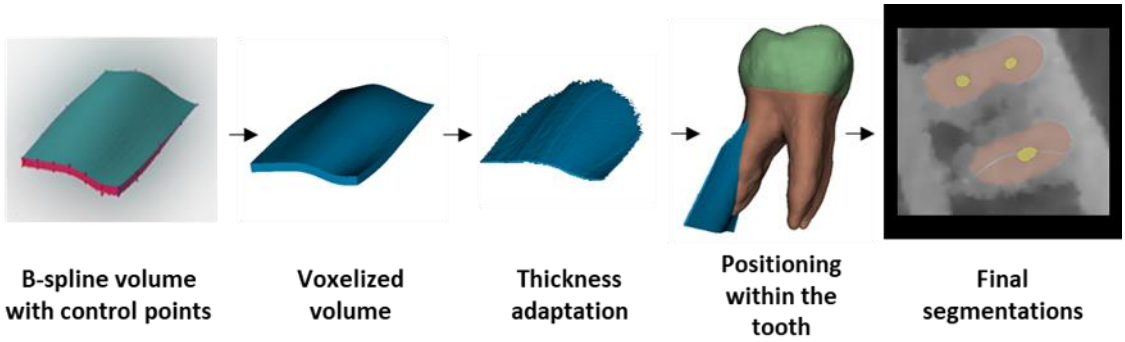

Figure 4. Illustration of the RF modelling procedure.

ii. Restorations

Three different types of dental restorations were selected for modelling: implants, fillings, and root canal treatments.

Dental implants were not self-developed as models of real implants are freely available online. A dental implant model along with the adjoining abutment and a screw retained crown were downloaded[39], followed by assembly, and voxelization (0.05 mm) using the 3D Slicer software.

Dental fillings come in various shapes, sizes, and positions. A database of different fillings was constructed based on examples found in clinical images. A filling was modelled by manually cutting out part of the dentin and enamel segments and smoothing the surface, thereby mimicking the shapes of the fillings from the examples. Logical operators were applied to obtain all the final segments for the tooth model with filling.

Two types of root canal treatments (RCT) were modelled: one using a prefabricated post and another one with a casted post. The steps performed during the clinical procedure were used as a guide. Figure 5 shows the modelling workflow for the two types of RCT. For the RCT with a prefabricated post (Figure 5a), a cylinder, with a 0.6 mm radius and adjustable length, was placed at the correct position within the pulp and dentin segments to represent the post. Next, the core, which is meant to seal the opening made in the tooth for the treatment, was modelled. A core is actually a dental filling, and therefore modelled as such. The post and core were then subtracted from the pulp segment. The remaining part of the pulp represented gutta-percha, the material used to fill the root canal after a RCT. Optionally, an artificial crown could be modelled, for which the enamel segment was used. For the casted post RCT (Figure 5b), a custom-made post with a core was modelled within the pulp and dentin segments. The remainder of the pulp segment represented again gutta-percha. For this type of RCT, a crown was modelled by

default using the enamel segment. Finally, for both types of RCT, logical operators were needed to obtain the final segments.

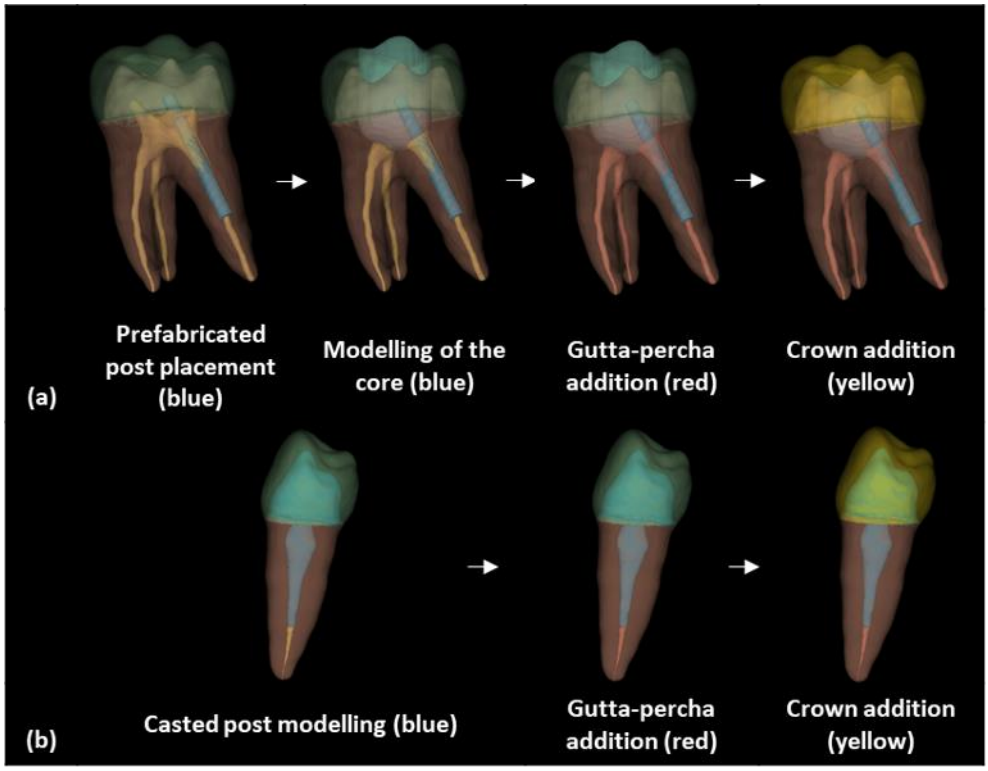

Figure 5. Workflow for RCT modelling, (a) with a prefabricated post and (b) with a casted post, illustrated in 3D view.

c. CBCT Simulation

Synthetic CBCT images of the developed model were created using an in-house developed simulation framework. A specific simulation strategy was applied to deal with the multi-resolution nature of the model. The simulated images were used in the validation study of the model.

i. Simulation framework

The framework includes all the elements of the CBCT imaging chain: the x-ray source, the rotational projection, the detector, and the image reconstruction. A 3D Accuitomo 170 (Morita, Japan) dental CBCT system was modelled in this study. The system is equipped with a fixed bowtie-like filter, whose exact shape was not specified, and a 19x24 cm flat panel indirect conversion detector with a CsI scintillator coupled to an a-Si photodiode array. The detector pixel size is 0.127x0.127 or 0.254x0.254 mm, depending on the operation mode. No anti-scatter grid is used. The x-ray source-to-rotation axis distance (SAD) is 54 cm. Depending on the selected FOV (there are nine options), the detector has two possible positions with source-to-detector distances (SDDs) of 74.4 cm or 84.2 cm, leading to respective geometric magnification factors of 1.38 and 1.56. The radiation coverage is always symmetrical, i.e., the central beam runs perpendicular to the detector center.

Source modelling was based on the equivalent source model (ESM) concept, which was introduced to overcome the need for manufacturer proprietary data that would be required for accurate simulation of the x-ray tube[40]. The ESM includes the energy spectrum of the x-ray beam and weighting factors reflecting the attenuation of the x-rays when crossing the tube filtration from different paths. The SPEKTR tool[41] was used to estimate the x-ray spectrum based on the clinical tube voltage of 90 kVp, and the measured half-value layer at the center of the x-ray beam. The effect of the bowtie-like filter was simulated by assigning a weighting factor to each primary photon (and all the secondary particles generated) depending on the photon's energy and take-off direction. The weighting factors reflect the attenuation through the filter, matching the physical scenario. They were determined from a raw flood image, available on the real system for flat-field correction calibration, showing the true x-ray intensity profile. Scatter within the bowtie-like filter was not considered, as it was assumed that scattered radiation from within the filter would not reach the detector[42]. A point source was modelled. The anode heel effect was not simulated as the variation in the radiation field would be much smaller compared to the variation caused by the bowtie-like filtration.

High resolution, noise free primary projections were determined according to the Beer-Lambert law by taking the exponential of the radiological path length through the object, representing the probability that a photon reaches the detector without absorption or angular deflection. Siddon's ray-tracing algorithm[43] was implemented for calculation of the radiological path length through the object. For an object with N^3 voxels, the algorithm scales with $3N$ instead of N^3 as it calculates the intersections of the rays with three orthogonal sets of equally spaced, parallel planes rather than intersections with the individual voxels. Ray-tracing was performed for 512 equally spaced projection angles over the full rotation trajectory, and at discrete energies with an interval of 5 keV over the energy range of the x-ray spectrum. At projection angle θ, the total attenuation through a 3D voxelized object observed in each detector pixel (x_{det},y_{det}) is then given by

$$A(x_{det}, y_{det}, \theta, E) = e^{-\sum \mu(x,y,z,E) l(x,y,z,\theta)} \quad (1)$$

with l the path length in cm traversed within each voxel (x,y,z) by the source-to-detector pixel ray, and μ the linear attenuation coefficient of the voxel material at energy bin E in cm^{-1}. For each of the simulated energies, the result was multiplied with a flood image, i.e., an image without an object. For the case of a perfect energy absorbing detector as simulated here, the flood image is equivalent to the energy fluence normalized to the initial number of simulated photons, in units of eV/cm²/photon. The primary projections are then expressed in the same units as the output of the scatter simulations (mentioned below), ensuring a consistent magnitude of the primary relative to the scatter projections. The flood image is independent of the projection angle. The expression to calculate each pixel value (x_{det},y_{det}) of the flood image was derived using the radiance theorem,

$$F(x_{det}, y_{det}, E) = \frac{nE}{\Omega_{source}} \Omega_{target} x \frac{1}{A_{target}} x \frac{1}{n} = \frac{E}{\Omega_{source}} \frac{SDD}{(x_{det}^2 + y_{det}^2 + SDD^2)^{3/2}} \quad (2)$$

with n the number of simulated photons, E the photon energy in eV, Ω_{source} the solid angle of the source in sr, Ω_{target} the solid angle of the target (i.e., the detector pixel) in sr, A_{target} the area of the detector pixel in cm², and SDD the source-to-detector distance in cm. The expression in equation 2 before the first multiplication sign denotes the energy deposited in each detector pixel. Spatial energy variations within one detector pixel were neglected as the detector pixels are sufficiently small. The x-rays were sent out uniformly in a rectangular beam (i.e,. a right-angled rectangular pyramid), modelling the x-ray collimators implicitly. For a right-angled pyramid, the solid angle is given by

$$\Omega_{source} = 4 \sin^{-1}(\sin\frac{\alpha}{2} \sin\frac{\beta}{2}) \quad (3)$$

with α and β the pyramid aperture angles. The aperture angles determine the size of the rectangular FOV on the detector plane.

The final primary projections were obtained by taking the weighted sum of the projection images at the different energies to reflect the x-ray spectrum,

$$P(x_{det}, y_{det}, \theta) = \sum_{i=1}^{N_E} w(E_i) F(x_{det}, y_{det}, E_i) A(x_{det}, y_{det}, \theta, E_i) \quad (4)$$

with N_E the number of energy bins, $w(E_i)$ the spectrum weighting factor at energy E_i, F the flood image at energy E_i, and A reflects the attenuation through the object at energy E_i.

Scattered radiation was generated using the PENELOPE/penEasy Monte Carlo transport code[44,45] and added to the total primary projections. Scatter image pixel values were expressed in eV/cm²/photon, matching the units of the primary projection images. To reduce computation time, a method for accelerated simulation of scatter projections was applied. Noisy scatter distributions were obtained by coarse MC simulations (5.10^8 histories/projection), and then denoised using Richardson-Lucy fitting[46,47].

Tissue compositions and densities for the different phantom tissues were taken from the ICRP 110[13] adult female phantom. However, for very specific dental structures, i.e., dentin, enamel, and the PLS, as well as the restorative

materials, the ICRP does not provide material characteristics. Therefore, for these materials, elemental compositions and density values were based on literature and manufacturer safety data sheets.
The total mass attenuation coefficient for each material was calculated based on the elemental composition using NIST data[48],

$$\frac{\mu}{\rho} = \sum_i w_i \left(\frac{\mu}{\rho}\right)_i \quad (5)$$

with w_i the fraction by weight and $\left(\frac{\mu}{\rho}\right)_i$ the mass attenuation coefficient of the ith atomic constituent in $\frac{cm^2}{g}$. The total attenuation coefficient in cm^{-1} was then given by multiplication of the mass attenuation and density values, and provided as input to the simulation framework.

Next, real system blurring and noise were added to the combined primary and scatter projections. Blurring and noise were quantified by respectively the presampling modulation transfer function (MTF) and the noise power spectrum (NPS). These metrics were measured from the 'For Processing' projection images accessible on the Accuitomo system, using the clinical tube voltage of 90 kVp. An additional 7 cm PMMA combined with 5.5 mm Al of beam filtration was placed at the x-ray tube exit to produce an x-ray spectrum consistent with that exiting an adult patient head. The MTF was measured using the slanted edge method[49] from images acquired at the highest load (175 mAs) to limit the influence of image noise on the measurement. The edge was placed at the isocenter to include both detector blurring and focal spot blurring, since the effect of the finite size of the focal spot was not yet included in the simulations. Figure 6a and b show the measured horizontal and vertical 1D MTF curves, and the resulting combined 2D MTF respectively. The NPS was measured from flood images acquired at different dose levels by varying the load between 17.5 and 123 mAs. Figure 6b shows radially averaged 1D normalized NPS (NNPS) curves at different dose levels. The total NPS was separated into electronic and quantum noise components[50]. Detector characteristics were then applied to the simulated images as follows: first, the images were convolved by the 2D MTF to obtain images with a realistic level of image blur. A noise image containing electronic and quantum noise relevant to the signal level being simulated at the x-ray detector was then generated[51,52]. The final simulated projection images were obtained by adding the blurred and total noise images together.
Finally, the total projection images were divided by the simulated flood image, similar as how the real scanner outputs projection data, and the natural logarithm was taken. Images were then reconstructed using the classical FDK algorithm[53,54]. After application of the ramp filter a Hann smoothing window was applied to suppress the highest spatial frequencies limiting artefacts caused by aliasing and noise.

Simulations were performed using supercomputing resources (Genius Tier-2 cluster). Cascadelake thin nodes, each consisting of 2 Xeon Gold 6240 CPUs@2.6 GHz containing 18 cores each, and 192 GB RAM were used. GPU computing was not applied.

Validation of the imaging chain was performed in the 'For Processing' projection images, as in the projection domain there is a linear relationship between exposure at the detector and pixel value in the projection image. Signal-difference-to-noise ratio (SDNR) was compared between the simulated and real images of a test object composed of a 16 cm thick PMMA block of 18x24 cm², which is the standard equivalent thickness of an adult head, with a 2 mm thick Al detail of 10x10 mm². SDNR was measured in the projection at the most perpendicular angle to the incident plane of the phantom, and calculated as follows

$$SDNR = \frac{PV_{obj} - PV_{bg}}{\sigma_{bg}} \quad (6)$$

with PV_{obj} the mean PV of nine 5x5 mm² regions of interest (ROIs) within the Al detail, and PV_{bg} the mean PV of twelve 5x5 mm² ROIs selected in two 10x10 mm² ROIs in the PMMA background of which the center was positioned at 15 mm from the center of the Al detail, both at the left and right side of the Al detail. σ_{bg} is the mean standard deviation in the PMMA background, calculated using the same ROIs as for PV_{bg}. The validation was performed at 90 kVp tube voltage, for three different dose levels (using tube loads of 61.3, 87.5, and 131.3 mAs). Relative deviations between the real and simulated SDNR values were below 10%.

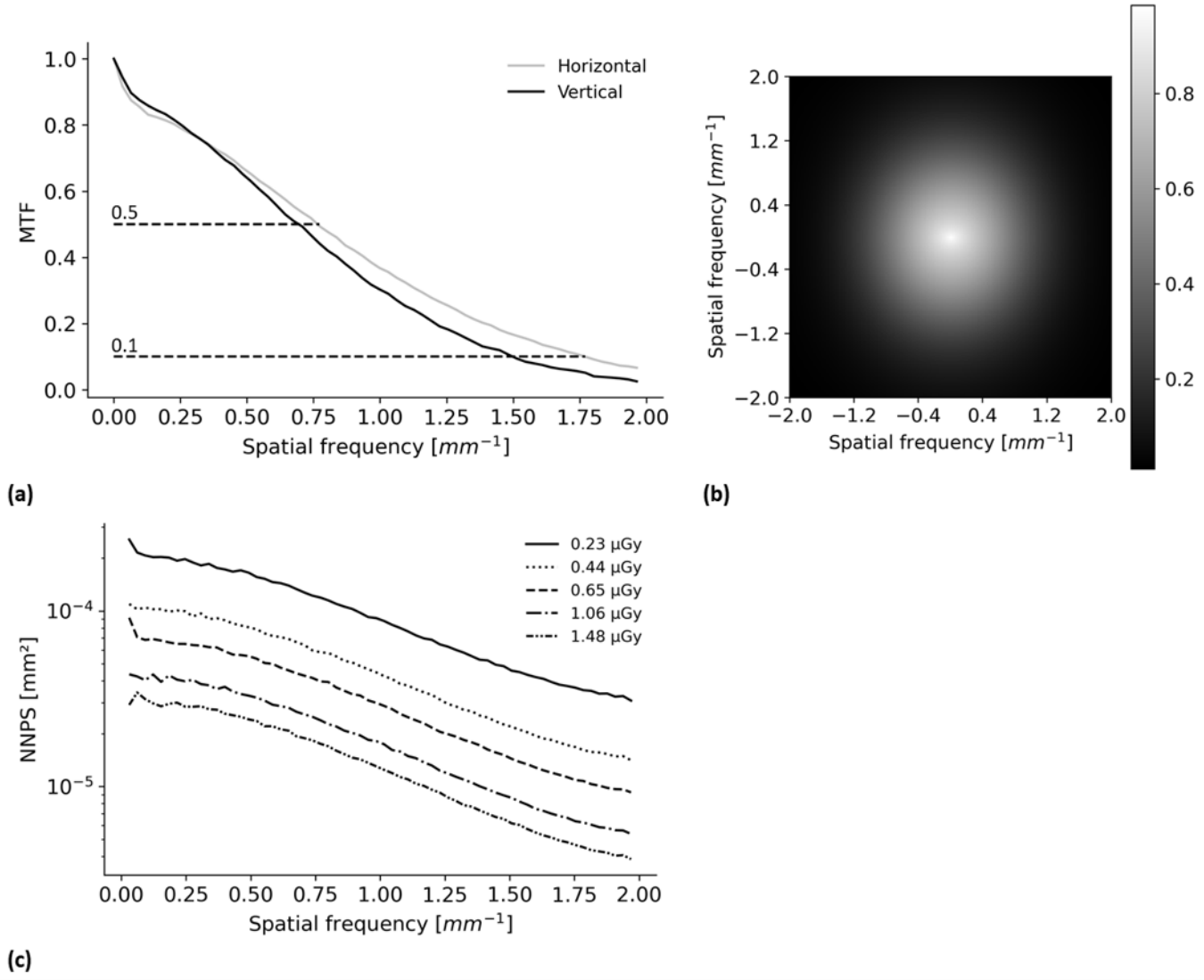

Figure 6. The measured resolution and noise characteristics, (a) the measured horizontal and vertical 1D MTF curves (the dashed lines indicate the 10% and 50% crossings), (b) the resulting combined 2D MTF, and (c) the radially averaged 1D NNPS curves measured at different dose levels. All the curves are visualized up to the Nyquist frequency.

ii. Multi-resolution phantom simulation

As the ray-trace and MC software can only handle single-resolution models, the developed multi-resolution phantom, consisting of a 0.2 mm resolution toothless head phantom (i.e., the base phantom) in which higher resolution tooth models of 0.05 mm were inserted, could not be fed directly into the simulation framework. Therefore the following procedure was applied to generate the primary and scatter projections.

The simulation procedure for the primary projections is illustrated in Figure 7. The first step in the simulation approach consisted of selecting distinct VOIs in the base phantom ensuring all teeth would be included. Therefore, the tooth models were downsampled to 0.2 mm resolution and inserted into the base phantom. In this phantom, six VOIs were selected, and the coordinates recorded (Figure 7a). The selected VOIs were then cropped from the toothless base phantom. Figure 7b shows an axial view of one of these six cropped VOIs (VOI 1, 4x zoom), as well as the cropped base phantom. The next step consisted of inserting the high resolution tooth models into the appropriate VOI in the desired configuration (e.g. normal anatomy, RFs, dental restorations, etc.). The resolution of the cropped VOIs was therefore first increased from 0.2 mm to 0.05 mm to allow a smooth transition between the teeth and the surrounding structures. Figure 7c shows an axial view of VOI 1 before and after tooth insertion, illustrated for the normal anatomy. The position offset of the center of each VOI from the center of the base phantom was calculated and used as input for the ray-trace software to shift the VOI to its correct position. Ray-tracing was performed separately on the high resolution VOIs and the cropped base phantom. For each discrete energy, the total attenuation through the complete head phantom was then obtained as follows,

$$A(x_{det}, y_{det}, \theta, E) = \prod_{i=1}^{N_i} A_i(x_{det}, y_{det}, \theta, E) \,.\, A_{base,cropped}(x_{det}, y_{det}, \theta, E) \quad (7)$$

with N_i the number of high resolution VOIs, i.e., 6. This is illustrated in figure 7d. The simulation procedure as described in the previous section could then be continued.

For simulation of the scattered projections, the phantom containing the downsampled tooth models was used. As scattered radiation is typically a slowly varying signal, it was not expected to be sensitive to details of anatomical structures[55].

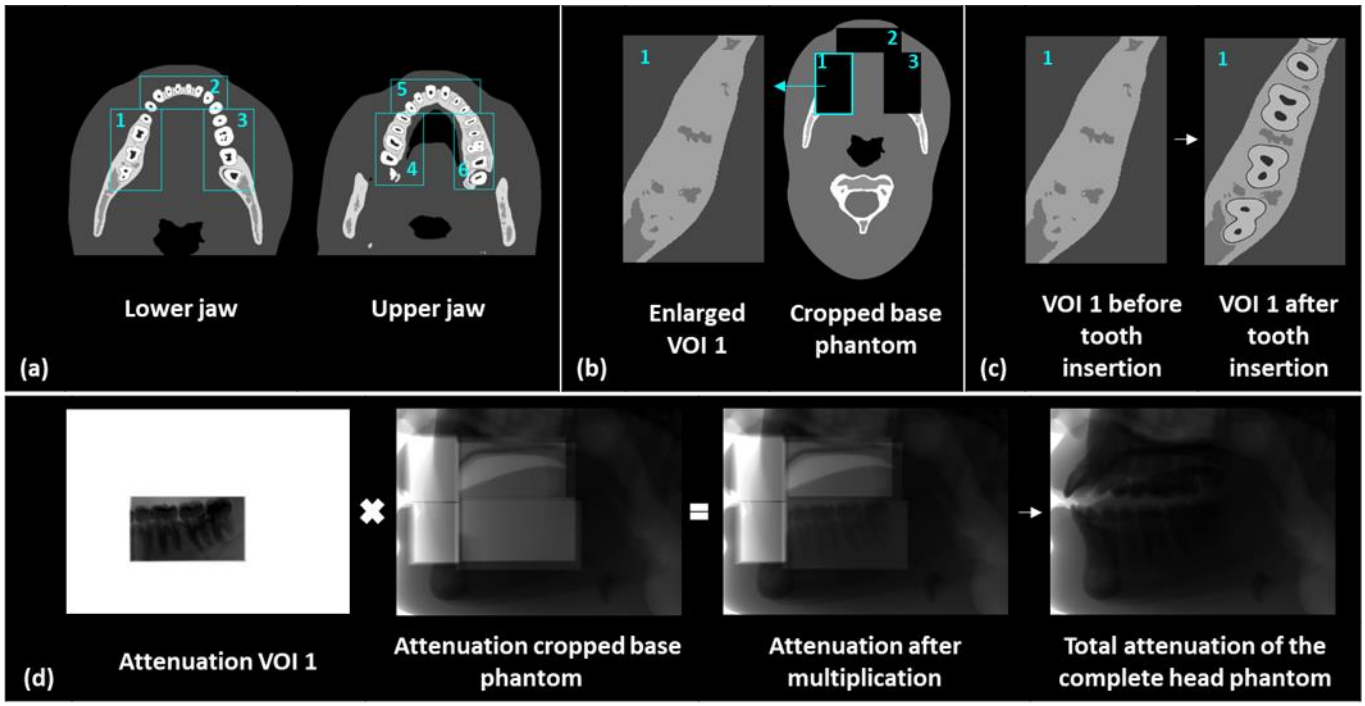

Figure 7. Illustration of the primary projection simulation procedure for the multi-resolution phantom, (a) VOI selection, (b) axial view of one of the cropped VOIs (VOI 1, 4x zoom), as well as the cropped base phantom, (c) axial view of VOI 1 upsampled, before and after tooth insertion, and (d) attenuation of VOI 1, the cropped base phantom, and the result after multiplication, as well as the total attenuation of the complete head phantom. The projection view shown was simulated at 75 keV.

d. Model validation

To validate the realism of the model anatomy as well as the associated clinical tasks, anatomical measurements were performed along with a reader study.

i. Anatomical measurements

Anatomical measurements of the dental structures as well as the mandible were assessed. All the measurements were carried out in 3D Slicer by a single user.

Regarding the dental structures, six measurements were performed in total on each tooth voxel model: five different tooth lengths and the pulp volume. Figure 8a illustrates the five different tooth length measurements; the tooth length, the crown length, the root length, and the mesiodistal and buccolingual diameters of the crown. For the pulp volume measurements on multi-rooted teeth, only the volume of the pulp chambers was measured. Therefore, roots were cut off manually from the pulp volumes.

Turning to the mandible, eight types of measurements were performed, illustrated in Figure 8b: the intergonial distance, the intercondylar distance, the body width, the pogonion-interdental distance, the body height, the body length, the ramus height, and the pogonion-lateral condyle distance.

All measurements were compared to mean reference values, and size ranges reported in literature[30,31,56]. Reference tooth length data were taken from a study[30] on 2393 maxillary and 2180 mandibular physical teeth. The pulp volume measurements[56] used as reference were measured on segmented pulp volumes in CBCT scans of 240 patients. For multi-rooted teeth, only pulp chamber volumes were provided to avoid the influence of the complexity

of the root canal system. Reference data for mandibular dimensions were taken from measurements on segmented mandibles from 65 CBCT scans[31].

Intra-observer reproducibility was assessed by repeating four times the six tooth measurements on a mandibular first molar, as well as the body height measurement on the mandible. For each measurement type, the mean and standard deviation, as well as the relative deviation from the mean for each of the four repeated measurements was calculated.

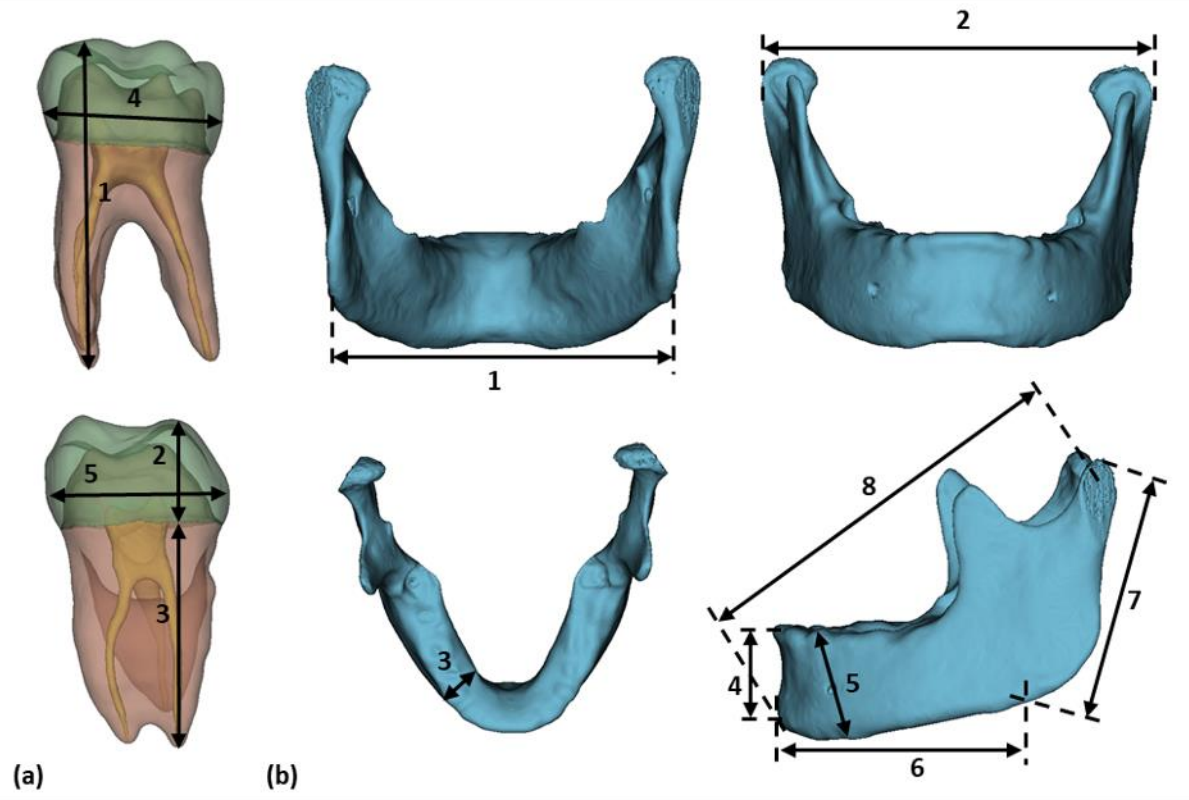

Figure 8. The anatomical measurements performed for model validation, (a) the tooth measurements illustrated on a mandibular first molar model; 1: tooth length, 2: crown length, 3: root length, 4: crown mesiodistal diameter, and 5: crown buccolingual diameter, and (b) the mandibular measurements; 1: intergonial distance, 2: intercondylar distance, 3: body width, 4: pogonion-interdental distance, 5: body height, 6: body length, 7: ramus height, 8: pogonion-lateral condylar distance.

ii. Reader study

A reader study[11] was set-up to assess the realism level of the normal anatomy of the model, as well as the pathosis (seven types of RFs), and the modelled restorations (five fillings, one implant, and three RCTs). In addition, for the modelled restorations, the realism level of the generated artefacts was also scored.

The RFs were modelled in frontal as well as posterior teeth. RFs often occur in endodontically treated teeth. However in this study, the RFs were modelled in healthy teeth to avoid metal artefacts from interfering with the RF visibility, allowing to score their appearance and positioning. Five simulated images, each containing a different combination of inserts, were simulated using a medium FOV size (11x8 cm²) with a reconstructed voxel size of 0.125 mm, a typical resolution used for diagnosis in endodontics. In clinical practice, only small FOVs are reconstructed at this high resolution. However, for this study, a larger FOV size was preferred to be able to evaluate the realism of all the important anatomical structures and tasks at once, to reduce the number of images that needed to be scored by the readers. A higher resolution than in clinical practice for this FOV size was then simulated to still be able to evaluate the fine structures that would be visible in the high resolution small FOV scans. Additionally, images were simulated at a dose level three times higher than the clinical level to reduce the influence of noise on the evaluation of the model. Images were generated at 90 kVp, as in clinical practice.

Two oral radiologists, each with 10 years of experience, scored the realism level of the developed models, as presented in Table 1, from the simulated images. For scoring, the five-point scale shown in Table 2 was used[11]. The position of the tasks was indicated, as the purpose of the study was to assess model realism, and not to conduct a search study. The readers were also informed that the dose level, as well as the resolution for a medium FOV size

scan were higher than in clinical practice. Contrast and brightness levels could be adjusted, there was no time limitation, and the images could be viewed in the axial, sagittal and coronal directions. Readers could also describe potential future improvements to the models. Due to the subjective nature of the study, a third expert oral radiologist with more than 20 years of experience was involved in cases of disagreement between the two readers.

Table 1. Overview of the questions scored in the reader study.

	Question	Realism level of
Normal anatomy	1	the teeth (enamel, dentin, pulp, PLS, LD)
	2	the background (mandible, maxilla, incisive canal, mandibular canals, soft tissues, air structures)
Pathosis	3	the RFs in terms of appearance (shape)
	4	the RFs in terms of position
Restorations	5	the dental fillings
	6	the dental implant
	7	the RCTs
	8	the artefacts

Table 2. Confidence levels

Five-point scale	Confidence level
1	Not at all realistic: critical elements that reduce the realism
2	Poor: obvious elements that reduce the realism
3	Adequate: minor elements that reduce the realism
4	Good: minimal amount of unrealistic elements
5	Very realistic: no unrealistic elements

III. RESULTS

a. Anthropomorphic voxel phantom with clinical tasks

Figure 9 shows a visual representation of all the modelled anatomical structures, without RFs and restorations.

Figure 10 shows examples of the modelled RFs and restorations (implant, fillings, and RCTs).

b. Model validation

i. Anatomical measurements

Tables 1A, 2A, and 3A show the results of the intra-observer reproducibility test for respectively the tooth length measurements, the pulp volume measurement, and the mandible body height measurement. For all measurement types evaluated, relative deviations from the mean value were maximally 2.3%, and could therefore be considered reproducible.

The results of the tooth length measurements, together with the corresponding literature reference values are shown in Tables 4A and 5A. The teeth are listed by their tooth number, using the universal numbering system[57], and ordered according to tooth type. All measurements were within the reference size range and showed relative deviations of less than 20% from the mean reference values. Deviations were less than 10.1% in 77% of all the measurements, and within 5.1% in 43% of the measurements.

The measured and reference pulp volumes are shown in Table 6A. All the segmented pulp volumes were within the reference minimum-maximum volume range, and within one standard deviation of the reference mean value. Table 7A shows the measured and reference mandible measurements. All measurements were within one standard deviation of the reference mean value.

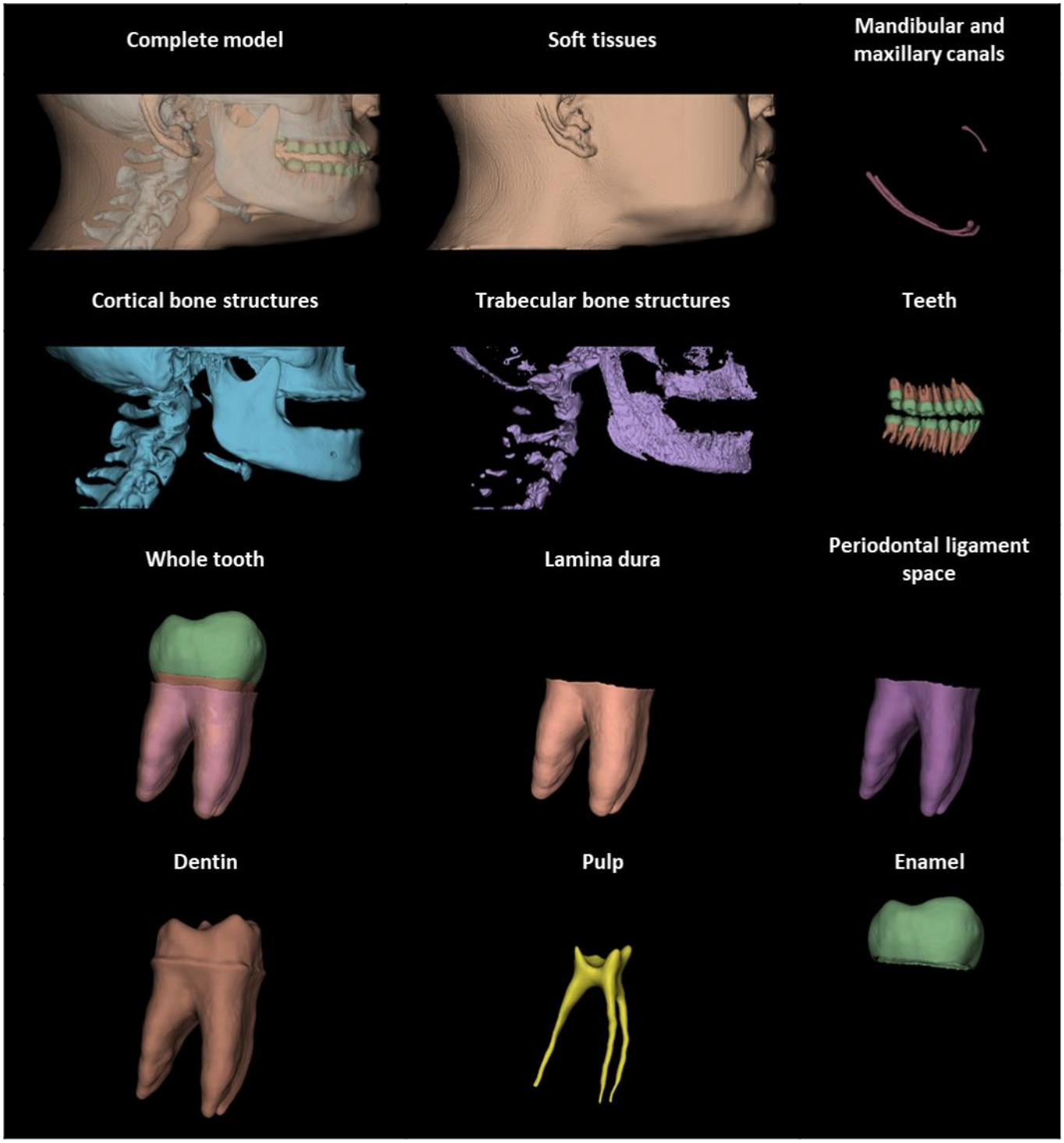

Figure 9. Overview of all the modelled anatomical structures within the anthropomorphic voxel model.

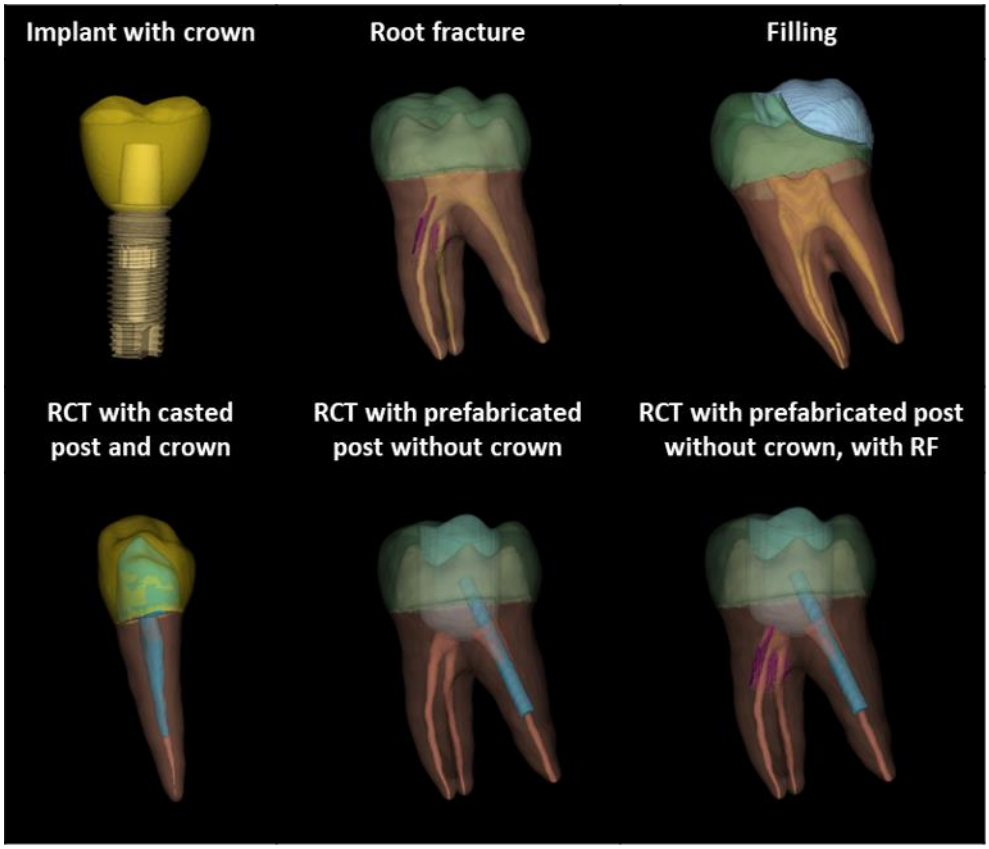

Figure 10. Examples of the modelled root fractures (RFs) and dental restorations (implants, fillings, root canal treatments (RCTs)).

ii. Reader study

Figure 11 shows one view of each of the simulated CBCT images used in the reader study. The images were created following the procedure described in section II.c. Ray-tracing of the high resolution crops took only about 10% of the simulation time of the cropped base phantom for the selected medium FOV size.

Regarding the normal anatomy of the model, both readers scored the anatomy of the teeth as good, and the realism of the background as less than adequate.

For the modelled pathosis i.e., the RFs, and the restorations, an overview of the reader results is shown in Table 3. The seven modelled RFs were scored by appearance and position. As for appearance, 100% and 57% of the RFs were scored at least adequate by reader 1 and 2 respectively, of which respectively 43% and 57% was scored at least good. Regarding the position, respectively 86% and 57% of the RFs were scored at least adequate by readers 1 and 2, of which 0% and 43% received a score of at least good. Reader 2 scored the same cases (43%) less than adequate both for appearance and position. In total, all the modelled RFs were scored at least adequate by at least one reader for appearance as well as position. In 57% of the cases both readers disagreed about the realism level of the RF position. Following evaluation by the third reader, it was concluded that RF realism was at least adequate for all. As for the restorations, all dental fillings were scored at least adequate, of which 80% and 100% were scored at least good by respectively reader 1 and 2. All the modelled RCTs were scored at least good by both readers. Realism of the implant model was also considered to be good. Finally, both readers agreed that realistic artefacts were produced by the modelled restorations.

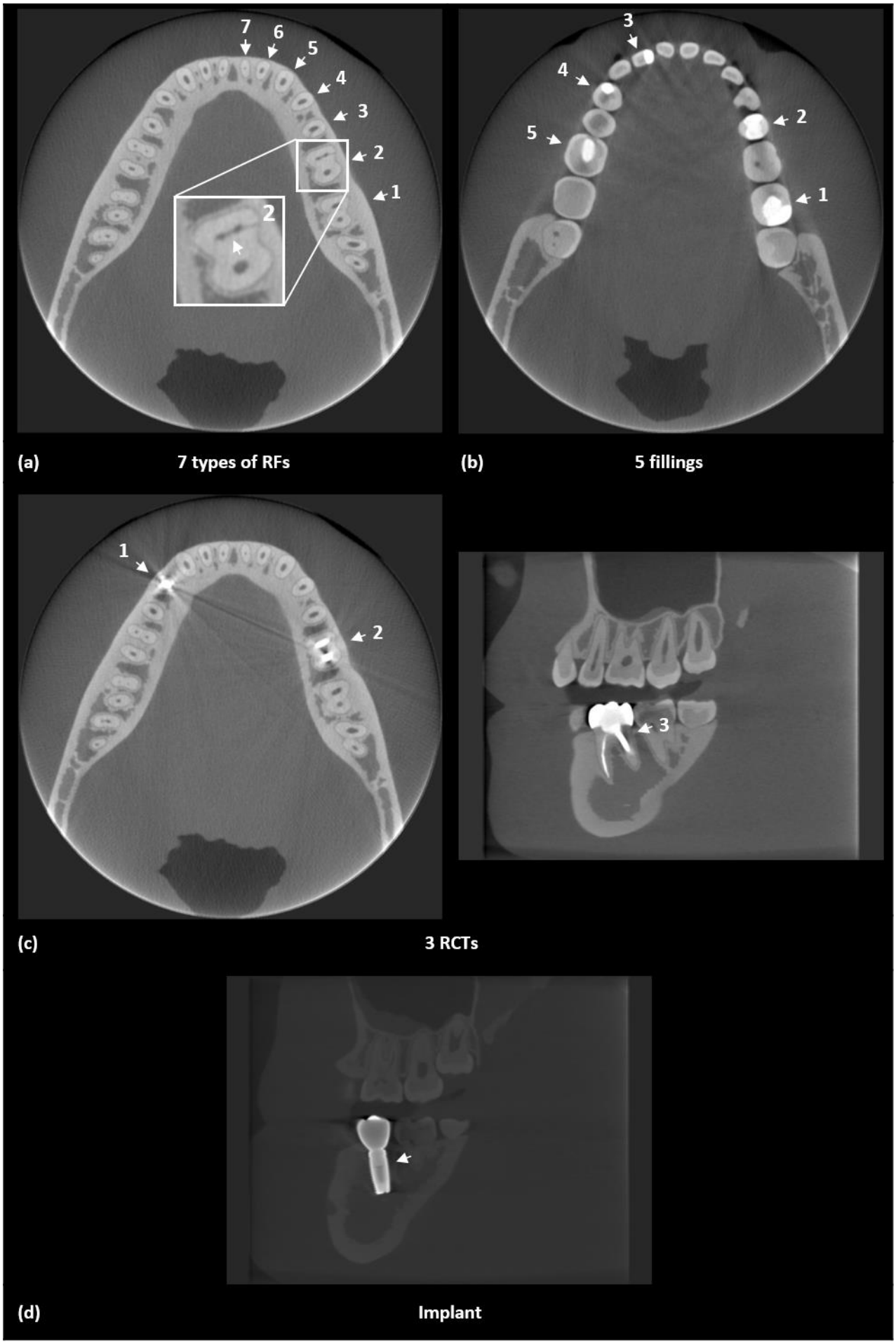

Figure 11. One view (axial or sagittal for visualization purposes) of the simulated CBCT images used in the reader study, showing (a) 7 RFs (with enlarged view of one of the modelled RFs), (b) 5 fillings, (c) 3 RCTs (1:casted post, 2: prefabricated post without

crown, 3: prefabricated post with crown), and (d) the implant model. The numbers and arrows indicate the tooth in which the RFs or the restorations were modelled. The realism level of the normal anatomy was scored from the remaining structures. The window level in the images was chosen for proper visualization of the inserts.

Table 3. Overview of the reader study results for the modelled pathosis and restorations. The table shows for each reader the percentage of cases with a realism score of at least adequate (≥ 3) and at least good (≥ 4).

		Pathosis		**Restorations**		
		RF appearance	*RF position*	*Filling*	*implant*	*RCT*
Number of cases scored		*7*		*5*	*1*	*2*
Reader 1	≥ 3	100%	86%	100%	100%	100%
	≥ 4	43%	0%	80%	100%	100%
Reader 2	≥ 3	57%	57%	100%	100%	100%
	≥ 4	57%	43%	100%	100%	100%

IV. DISCUSSION

This work described a methodology for the development and validation of an anthropomorphic voxel phantom with associated clinical tasks for task-based image quality optimization studies in dental imaging research.

To generate the voxel phantom the relevant anatomical structures were segmented from clinical CBCT image data. Although several semi-automatic segmentation tools were used to speed-up the segmentation process, an experienced user required approximately 1.5 hours to segment a single tooth. Approximately 100 hours were needed for the segmentation of the surrounding structures and the merging of both patients, as many manual modifications were necessary. In order to segment specific dental structures and parts of the trabecular bone accurately, higher resolution images would be needed. As these images were not available, missing features had to be modelled. The decision not to model the trabecular bone structure in detail led to the development of a multi-resolution model, in which high resolution tooth models (0.05 mm) were inserted into a lower resolution head voxel phantom (0.2 mm). This reduced the model size significantly, and as a consequence the computational load in the simulations. The soft tissues of the phantom had to be segmented as a whole as it is not possible to differentiate between various soft tissues on a CBCT scan due to its poor low contrast resolution. Starting from head and neck CT scans was not considered in the frame of this work, as they do not exhibit high enough resolution for proper visualization of the dental structures. As a consequence, the developed phantom is currently suitable for image quality applications only. However, this is not really a downside, as dose estimates can be obtained from simulations using the already developed dosimetry phantoms.
Validation of the normal anatomy was partly assessed through measurements of tooth length, pulp volume, and the mandible and comparison with reference data from literature. The measurements were within 20% or one standard deviation from population mean reference values. In addition, a reader study was performed. Both oral radiologists agreed that the realism level of the teeth was good. The realism level of the background structures was scored less than adequate due to the lack of detailed enough trabecular bone structure, and any cortication of the mandibular canal for the simulated image resolution. This was expected, and detailed modelling of the trabecular bone structure based on its morphometry and 3D geometrical complexity will be the objective of future work, starting from related work described in literature[58,59]. This will allow to model bone pathoses as well. The realism of the spine and cranial bones was not assessed. However, although it was necessary to model these structures, their accuracy was less important within the global scope of the project.

In the context of task-based optimization, modelling of clinically interesting tasks was necessary. RF detection in the presence of metal artefacts was considered the main clinical task of interest. This led to the modelling of RFs and different dental restoration types. Positioning of the RFs and dental implant, as well as the modelling of the fillings and the RCTs required many manual interactions which could not be automated. Modelling and positioning

of a RF, positioning of the implant model, modelling a filling, and a RCT took approximately 1.5 hours, 30 min, 30 min, and 1.5 hours respectively, for an experienced user.
Regarding the realism of the RFs, in total, all the cases received a realism score of at least adequate by at least one of the readers in terms of both appearance and position. In 57% of the cases the readers disagreed about the realism level. Disagreement between readers is not uncommon in these types of study as the readers' score reflect their personal experience, and is therefore subjective. For this reason, a third expert oral radiologist was involved for the final decision. After discussion with the oral radiologists, it was clear that scores of less than adequate were obtained in cases where the chosen position for the RF was less common in clinical practice. In addition, the type of fracture modelled could also be less common in clinical practice, and some types are more often seen in anterior than in posterior teeth as well as the other way around. These elements were not considered during the design of the study. However, the mentioned reasons did not imply that the proposed procedure was not able to generate realistic RFs, and it was agreed that the developed methodology can be used further for RF modelling. For future studies, additional advice from oral radiologists, not participating in the final study, about common RF positions and types can be included while setting up a specific optimization study. At the moment, the RFs were simulated based on visual examples and literature information, without taking into account the different material properties of the dental structures and how they would interact due to externally applied forces inducing a RF. RF modelling can possibly be improved by moving toward finite element-based modelling. RF initiation and propagation can then be simulated for specific situations, e.g. simulations could be performed on a tooth model with RCT under different force loads[60], or on a healthy tooth model to simulate fracture formation due to trauma. The potential of finite element methods for RF formation can be investigated in future work. Additionally, when studying RFs, secondary bone destruction and periodontal ligament widening should also be considered.
Finally, regarding the modelling of different restoration types, both readers agreed that a good level of realism was achieved for both the models and the associated artefacts they produce.

A specific simulation strategy was applied to simulate the multi-resolution head phantom. An advantage of this simulation strategy was that, for a specific FOV and tube voltage, the ray-tracing of the cropped base phantom, which was the most time consuming, only had to be performed once. If other simulations of the phantom containing different dental configurations are to be simulated, only the VOIs with different inserts would have to be ray-traced additionally, speeding-up the simulation process considerably.
In addition, for image quality studies, high resolution phantoms are needed, which unavoidably increases the computational load, and hence the simulation time. Therefore, the concept of a multi-resolution model could be of interest. Structures of less clinical relevance for the study could be modelled in a lower resolution, reducing the phantom size and as a consequence the simulation time.

Currently, the developed model can be used for several types of optimization studies of clinical relevance. More specifically, studying the influence of x-ray acquisition parameters like tube current, tube voltage and filtration, or detector resolution on RF detectability. Furthermore, in dentistry, a variety of restorative materials is available, leading to different levels of artefacts in CBCT images. Exploring the influence of different restorative materials on RF detectability is also possible. Testing the effect of several data processing techniques, e.g. scatter correction methods, metal artefact reduction algorithms, or different reconstruction algorithms on RF visibility would also be a promising application for the developed model. With the inclusion of anti-scatter grid modelling in the platform, the influence of x-ray scattered radiation on task performance can be studied. There is also the opportunity to investigate new imaging technologies such as detectors for dual energy imaging in dental CBCT applications, with the potential to reduce beam hardening artefacts.
While it is possible to simulate variability in the dentition of the current model, a limitation when using this phantom is the lack of background anatomical variation. As a consequence, investigating the detectability of a specific pathosis within a clinical population containing male and female patients, a range of ages and ethnicities, as well as anatomical differences between individuals is not possible. In order to assess the impact of an imaging modality on a patient population, a range of phantoms covering the anatomical variation present in the population will have to be developed[7]. The difference in large scale anatomical variation that comes from including different patients will have influence on imaging performance, depending on the scope of the VIT. For the case of dental CBCT imaging, one could expect differences in x-ray transmission for different skulls sizes leading to variations in exposure

levels and scattered radiation intensity at the x-ray detector input plane. These in turn will introduce differences in background signal intensity and image noise. Turning to imaging of the teeth, some population specific variation can already be introduced by modelling the variation of dentition as discussed earlier. With regard to patient age, a longitudinal study[61] has shown that changes in dimensions of the order of 1 mm can be expected for subjects followed from early adolescence to middle age. In addition, when focusing on RF detection, the development of pediatric models has lower clinical relevance, as RF incidence is highest among adults[23]. Obviously, a population will contain female and male patients which have to be modelled and included. Looking at differences in models for female and male patients, morphometric measurements[31] of the mandible data show male dimensions to be 4 mm (or ~7%) larger, on average compared to female dimensions. Generation of a large number of such models was outside the scope of this project, where the focus lay on developing a methodology to produce a clinically relevant image quality model for dental imaging. The prototype model was designed to have dimensions close to the population average so that virtual imaging studies using this phantom would be relevant to a large proportion of the patient population.

If more models are to be developed, the workflow can be extended. First, instead of the time consuming manual and semi-automatic segmentation procedures, the use of fully automatic segmentation tools could speed-up the development of the model by providing a first rough segmentation of all the teeth and the cranio-maxillofacial structures. Currently, automatic segmentation tools for dental applications are being developed[62–65]. Nevertheless, to the best of the authors knowledge, these tools do not yet provide automatic root canal segmentation or separation between the enamel and the dentin, and many manual interactions would still be required. Second, the voxel phantom should be converted into a mesh or non-uniform rational B-spline model. Currently, the voxelized nature of the phantom limits its flexibility, in particular for modelling anatomical variation as well as patient motion. Including patient motion is also of particular interest for future applications in dental CBCT imaging. Besides the presence of highly dense restorations, it is one of the most important causes of image artefacts. Unlike clinical CT, dental CBCT imaging typically requires a longer scan time increasing the probability of patient movement. Like the metal streak artefacts, motion artefacts degrade image quality, negatively affecting diagnosis, e.g. of RFs, or treatment planning[54]. Currently, rigid motion, e.g. head rotation and translation, can be simulated. However, other types of motion which are not feasible with voxel phantoms are also of particular interest, e.g. jaw motion, nodding and tilting of the head, trembling, tongue motion, or swallowing, etc.

V. CONCLUSIONS

In this work, a methodology was described to develop an adult anthropomorphic head voxel phantom containing relevant clinical features for dental CBCT imaging. Segmentation and a-priori anatomical knowledge were used to create the model. The realism of the model was confirmed by quantitative measurements of anatomical structures and by oral radiologists who scored the realism level of the developed model and associated clinical tasks from simulated images. The model can form the basis for task-based image quality optimization studies of dental CBCT imaging, in particular for root fracture detection tasks. The methodology can be extended to create more models representative of the clinical population.

Acknowledgements

This work was supported by the Internal research fund of the Katholieke Universiteit Leuven (grant number C24/18/065). The computational resources and services used in this work were provided by the VSC (Flemish Supercomputer Center), funded by the Research Foundation Flanders (FWO) and the Flemish Government.

Conflict of interest

The authors have no conflicts of interest to disclose.

REFERENCES

1. Gaêta-Araujo H, Alzoubi T, de Faria Vasconcelos K, et al. Cone beam computed tomography in dentomaxillofacial radiology: a two-decade overview. *Dentomaxillofacial Radiol*. 2020;49. doi:10.1259/dmfr.20200145
2. Gaêta-Araujo H, Leite AF, de Faria Vasconcelos K, Jacobs R. Two decades of research on CBCT imaging in DMFR – an appraisal of

scientific evidence. *Dentomaxillofacial Radiol*. 2021;49. doi:10.1259/dmfr.20200367
3. Pauwels R, Beinsberger J, Stamatakis H, et al. Comparison of spatial and contrast resolution for cone-beam computed tomography scanners. *Oral Surg Oral Med Oral Pathol Oral Radiol*. 2012;114(1):127-135. doi:10.1016/j.oooo.2012.01.020
4. Pauwels R, Beinsberger J, Collaert B, et al. Effective dose range for dental cone beam computed tomography scanners. *Eur J Radiol*. 2012;81:267-271. doi:10.1016/j.ejrad.2010.11.028
5. Stratis A, Zhang G, Jacobs R, Bogaerts R, Bosmans H. The growing concern of radiation dose in paediatric dental and maxillofacial CBCT: an easy guide for daily practice. *Eur Radiol*. 2019;29:7009-7018. doi:10.1007/s00330-019-06287-5
6. Pinto JC, Wanderley VA, de Faria Vasconcelos K, et al. Evaluation of 10 Cone-beam Computed Tomographic Devices for Endodontic Assessment of Fine Anatomic Structures. *J Endod*. 2021;47(6):947-953. doi:10.1016/j.joen.2021.02.013
7. Abadi E, Segars WP, Tsui BMW, et al. Virtual clinical trials in medical imaging: a review. *J Med Imaging*. 2020;7(4). doi:10.1117/1.JMI.7.4.042805
8. Samei E, Kinahan P, Nishikawa RM, Maidment A. Virtual Clinical Trials: Why and What (Special Section Guest Editorial). *J Med Imaging*. 2020;7(4). doi:10.1117/1.jmi.7.4.042801
9. Xu XG. An exponential growth of computational phantom research in radiation protection, imaging, and radiotherapy: a review of the fifty-year history. *Phys Med Biol*. 2014;59:233-302. doi:10.1088/0031-9155/59/18/R233
10. Cassola VF, de Melo Lima VJ, Kramer R, Khoury HJ. FASH and MASH: female and male adult human phantoms based on polygon mesh surfaces: I. Development of the anatomy. *Phys Med Biol*. 2010;55:133-162. doi:10.1088/0031-9155/55/1/009
11. Rodríguez Pérez S, Coolen J, Struelens L, et al. Methodology to create 3D models of COVID-19 pathologies for virtual clinical trials. *J Med Imaging*. 2021;8(S1). doi:10.1117/1.JMI.8.S1.013501
12. Segars WP, Sturgeon G, Mendonca S, Grimes J, Tsui BMW. 4D XCAT phantom for multimodality imaging research. *Med Phys*. 2010;37(9):4902-4915. doi:10.1118/1.3480985
13. ICRP. Adult reference computational phantoms: ICRP publication 110. *Ann ICRP*. 2009;39(2):1-166.
14. Lombardo PA, Vanhavere F, Lebacq AL, Struelens L, Bogaerts R. Development and Validation of the Realistic Anthropomorphic Flexible (RAF) Phantom. *Health Phys*. 2018;114(5):486-499. doi:10.1097/HP.0000000000000805
15. Zhang G, Luo Q, Zeng S, Liu Q. The development and application of the visible Chinese human model for Monte Carlo dose calculations. *Health Phys*. 2008;94(2):118-125. doi:10.1097/01.HP.0000285256.48498.b4
16. Zubal IG, Harrell CR, Smith EO, Rattner Z, Gindi G, Hoffer PB. Computerized three-dimensional segmented human anatomy. *Med Phys*. 1994;21(2):299-302. doi:10.1118/1.597290
17. Christ A, Kainz W, Hahn EG, et al. The Virtual Family - development of surface-based anatomical models of two adults and two children for dosimetric simulations. *Phys Med Biol*. 2010;55:23-38. doi:10.1088/0031-9155/55/2/N01
18. Andreas S, Nathan T, Guozhi Z, et al. Development of a paediatric head voxel model database for dosimetric applications. *Br J Radiol*. 2017;90(1078):20170051. doi:10.1259/bjr.20170051
19. Iacono MI, Neufeld E, Akinnagbe E, et al. MIDA: A Multimodal Imaging-Based Detailed Anatomical Model of the Human Head and Neck. *PLoS One*. 2015;10(4). doi:10.1371/journal.pone.0124126
20. Bueno MR, Azevedo BC, Estrela C. A critical review of the differential diagnosis of root fracture line in CBCT scans. *Braz Dent J*. 2021;32(5):114-128. doi:10.1590/0103-6440202104742
21. Gaêta-Araujo H, Queiroz Silva de Souza G, Queiroz Freitas D, de Oliveira-santos C. Optimization of Tube Current in Cone-beam Computed Tomography for the Detection of Vertical Root Fractures with Different Intracanal Materials. *J Endod*. 2017;43(10):1668-1673. doi:10.1016/j.joen.2017.04.003
22. Gao A, Cao D, Lin Z. Diagnosis of cracked teeth using cone-beam computed tomography: literature review and clinical experience. *Dentomaxillofacial Radiol*. 2021;50. doi:10.1259/dmfr.20200407
23. Talwar S, Utneja S, Nawal RR, Kaushik A, Srivastava D, Oberoy SS. Role of Cone-beam Computed Tomography in Diagnosis of Vertical Root Fractures: A Systematic Review and Meta-analysis. *J Endod*. 2016;42(1):12-24. doi:10.1016/j.joen.2015.09.012
24. Pinto MGO, Rabelo KA, Sousa Melo SL, et al. Influence of exposure parameters on the detection of simulated root fractures in the presence of various intracanal materials. *Int Endod J*. 2017;50:586-594. doi:10.1111/iej.12655
25. Marinho Vieira LE, Diniz de Lima E, Peixoto LR, et al. Assessment of the Influence of Different Intracanal Materials on the Detection of Root Fracture in Birooted Teeth by Cone-beam Computed Tomography. *J Endod*. 2020;46(2):264-270. doi:10.1016/j.joen.2019.10.028
26. Pinto JC, De Faria Vasconcelos K, Ferreira Leite A, et al. *Image Quality for Visualization of Cracks and Fine Endodontic Structures Using 10 CBCT Devices with Various Scanning Protocols and Artefact Conditions*. Vol 13.; 2023. doi:10.1038/s41598-023-31099-5
27. Kapralos V, Koutroulis A, Irinakis E, et al. Digital subtraction radiography in detection of vertical root fractures: accuracy evaluation for root canal filling, fracture orientation and width variables. An ex-vivo study. *Clin Oral Investig*. 2020;24:3671-3681. doi:10.1007/s00784-020-03245-0
28. Fedorov A, Beichel R, Kalpathy-Cramer J, et al. 3D Slicer as an image computing platform for the Quantitative Imaging Network. *Magn Reson Imaging*. 2012;30:1323-1341. doi:10.1016/j.mri.2012.05.001
29. Vehkalahti MM, Palotie U, Valaste M. Age-related variation in volume and content of restorative private dental care for adults in Finland in 2012–2017: A nationwide register-based observation. *J Dent*. 2021;104:103537. doi:10.1016/j.jdent.2020.103537
30. Woelfel JB. *Woelfel's Dental Anatomy*. 8th ed. (Scheid RC, Weiss G, eds.). Wolters Kluwer/Lippincott Williams & Wilkins Health; 2012.
31. Vallabh R, Zhang J, Fernandez J, Dimitroulis G, Ackland DC. The morphology of the human mandible: A computational modelling study. *Biomech Model Mechanobiol*. 2020;19:1187-1202. doi:10.1007/s10237-019-01133-5
32. Gradient Anisotropic Diffusion — 3D Slicer documentation. https://slicer.readthedocs.io/en/latest/user_guide/modules/gradientanisotropicdiffusion.html. Accessed December 23, 2022.
33. Segment editor — 3D Slicer documentation. https://slicer.readthedocs.io/en/latest/user_guide/modules/segmenteditor.html. Accessed September 21, 2022.
34. Mortazavi H, Baharvand M. Review of common conditions associated with periodontal ligament widening. *Imaging Sci Dent*. 2016;46:229-237. doi:10.5624/isd.2016.46.4.229
35. Hubar JS. Quantification of the lamina dura. *J Can Dent Assoc*. 1993;59(12):997-1000.

36. Campello AF, Marceliano-Alves MF, Siqueira JF, et al. Determination of the Initial Apical Canal Diameter by the First File to Bind or Cone-beam Computed Tomographic Measurements Using Micro-computed Tomography as the Gold Standard: An Ex Vivo Study in Human Cadavers. *J Endod*. 2019;45(5):619-622. doi:10.1016/j.joen.2019.01.020
37. Guo XL, Li G, Zheng JQ, et al. Accuracy of detecting vertical root fractures in non-root filled teeth using cone beam computed tomography: effect of voxel size and fracture width. *Int Endod J*. 2019;52:887-898. doi:10.1111/iej.13076
38. Bingol OR, Krishnamurthy A. NURBS-Python: An open-source object-oriented NURBS modeling framework in Python. *SoftwareX*. 2019;9:85-94. doi:10.1016/j.softx.2018.12.005
39. Dental Implant model by dgailis - Thingiverse. https://www.thingiverse.com/thing:3574773. Accessed September 30, 2022.
40. Stratis A, Zhang G, Lopez-Rendon X, Jacobs R, Bogaerts R, Bosmans H. Customisation of a Monte Carlo dosimetry tool for dental cone-beam CT systems. *Radiat Prot Dosimetry*. 2016;169(1-4):378-385. doi:10.1093/rpd/ncw024
41. Siewerdsen JH, Waese AM, Moseley DJ, Richard S, Jaffray DA. Spektr : A computational tool for x-ray spectral analysis and imaging system optimization. *Med Phys*. 2004;31(11):3057-3067. doi:10.1118/1.1758350
42. Sharma S, Abadi E, Kapadia A, Segars WP, Samei E. A GPU-accelerated framework for rapid estimation of scanner-specific scatter in CT for virtual imaging trials. *Phys Med Biol*. 2021;66. doi:10.1088/1361-6560/abeb32
43. Siddon RL. Fast calculation of the exact radiological path for a three-dimensional CT array. *Med Phys*. 1985;12(2):252-255.
44. Sempau J, Badal A, Brualla L. A PENELOPE-based system for the automated Monte Carlo simulation of clinacs and voxelized geometries-application to far-from-axis fields. *Med Phys*. 2011;38(11):5887-5895. doi:10.1118/1.3643029
45. Salvat F, Fernández-Varea J, Acosta E, Sempau J. PENELOPE: A code system for Monte Carlo Simulation of Electron and Photon Transport. *Work Proc*. 2006:384. doi:10.1.1.78.4492
46. Zbijewski W, Beekman FJ. Efficient Monte Carlo Based Scatter Artifact Reduction in Cone-Beam Micro-CT. *IEEE Trans Med Imaging*. 2006;25(7):817-827. doi:10.1109/TMI.2006.872328
47. Baer M, Kachelrieß M. Hybrid scatter correction for CT imaging. *Phys Med Biol*. 2012;57:6849-6867. doi:10.1088/0031-9155/57/21/6849
48. X-Ray Mass Attenuation Coefficients | NIST. doi:10.18434/T4D01F
49. Samei E, Flynn MJ, Reimann DA. A method for measuring the presampled MTF of digital radiographic systems using an edge test device. *Med Phys*. 1998;25(1):102-113.
50. Mackenzie A, Honey ID. Characterization of noise sources for two generations of computed radiography systems using powder and crystalline photostimulable phosphors. *Med Phys*. 2007;34(8):3345-3357. doi:10.1118/1.2750973
51. MacKenzie A, Dance DR, Workman A, Yip M, Wells K, Young KC. Conversion of mammographic images to appear with the noise and sharpness characteristics of a different detector and x-ray system. *Med Phys*. 2012;39(5):2721-2734. doi:10.1118/1.4704525
52. Båth M, Håkansson M, Tingberg A, Månsson LG. Method of simulating dose reduction for digital radiographic systems. *Radiat Prot Dosimetry*. 2005;114(1-3):253-259. doi:10.1093/rpd/nch540
53. Feldkamp LA, Davis LC, Kress JW. Practical cone-beam algorithm. *J Opt Soc Am*. 1984;1(6):612-619. doi:10.1364/josaa.1.000612
54. Sun T, Jacobs R, Pauwels R, Tijskens E, Fulton R, Nuyts J. A motion correction approach for oral and maxillofacial cone-beam CT imaging. *Phys Med Biol*. 2021;66(12):125008. doi:10.1088/1361-6560/abfa38
55. Xu Y, Bai T, Yan H, et al. A practical cone-beam CT scatter correction method with optimized Monte Carlo simulations for image-guided radiation therapy. *Phys Med Biol*. 2015;60:3567-3587. doi:10.1088/0031-9155/60/9/3567
56. Ge Z, Yang P, Li G, Zhang J, Ma X. Age estimation based on pulp cavity/chamber volume of 13 types of tooth from cone beam computed tomography images. *Int J Legal Med*. 2016;130:1159-1167. doi:10.1007/s00414-016-1384-6
57. Universal Tooth Numbering System - Anomalies of Tooth Structure - Dentalcare. https://www.dentalcare.com/en-us/ce-courses/ce651/universal-tooth-numbering-system. Accessed December 12, 2022.
58. Abadi E, Segars WP, Sturgeon GM, Harrawood B, Kapadia A, Samei E. Modeling "Textured" Bones in Virtual Human Phantoms. *IEEE Trans Radiat Plasma Med Sci*. 2019;3(1):47-53. doi:10.1109/TRPMS.2018.2828083
59. Abadi E, Segars WP, Sturgeon GM, Roos JE, Ravin CE, Samei E. Modeling Lung Architecture in the XCAT Series of Phantoms: Physiologically Based Airways, Arteries and Veins. *IEEE Trans Med Imaging*. 2018;37(3):693-702. doi:10.1109/TMI.2017.2769640
60. Ramezani M, de Las Casas EB, de Almeida Mattos CM, Manzoli OL, Rodrigues EA. Finite element simulation of fracture in a restored premolar tooth using high aspect ratio elements. *Res Biomed Eng*. 2018;34(1):54-64. doi:10.1590/2446-4740.05817
61. Tsiopas N, Nilner M, Bondemark L, Bjerklin K. A 40 years follow-up of dental arch dimensions and incisor irregularity in adults. *Eur J Orthod*. 2013;35:230-235. doi:10.1093/ejo/cjr121
62. Verhelst P-J, Smolders A, Beznik T, et al. Layered deep learning for automatic mandibular segmentation in cone-beam computed tomography. *J Dent*. 2021;114. doi:10.1016/j.jdent.2021.103786
63. Shaheen E, Leite A, Alqahtani KA, et al. A novel deep learning system for multi-class tooth segmentation and classification on cone beam computed tomography. A validation study. *J Dent*. 2021;115. doi:10.1016/j.jdent.2021.103865
64. Lahoud P, Diels S, Niclaes L, et al. Development and validation of a novel artificial intelligence driven tool for accurate mandibular canal segmentation on CBCT. *J Dent*. 2022;116. doi:10.1016/j.jdent.2021.103891
65. Morgan N, Van Gerven A, Smolders A, de Faria Vasconcelos K, Willems H, Jacobs R. Convolutional neural network for automatic maxillary sinus segmentation on cone-beam computed tomographic images. *Nat Sci Reports*. 2022;12:1-9. doi:10.1038/s41598-022-11483-3

APPENDIX

Table 1A. Tooth length reproducibility measurements on a mandibular first molar.

	Tooth length				Crown length				Root length				Mesiodistal diameter				Buccolingual diameter			
	Length [mm]	Mean [mm]	SD [mm]	Relative error [%]	Length [mm]	Mean [mm]	SD [mm]	Relative error [%]	Length [mm]	Mean [mm]	SD [mm]	Relative error [%]	Diameter [mm]	Mean [mm]	SD [mm]	Relative error [%]	Diameter [mm]	Mean [mm]	SD [mm]	Relative error [%]
1	24.01	24.04	0.037	-0.1	11.98	11.99	0.021	-0.1	12.73	12.68	0.036	0.4	9.01	9.04	0.036	-0.3	7.42	7.45	0.032	-0.3
2	24.08			0.2	11.97			-0.2	12.66			-0.1	9.09			0.6	7.42			-0.4
3	24.00			-0.1	12.01			0.1	12.65			-0.2	9.02			-0.2	7.47			0.3
4	24.05			0.1	12.01			0.1	12.67			-0.1	9.04			0.0	7.48			0.4

SD = standard deviation

Table 2A. Reproducibility of the pulp volume measurement in multi-rooted teeth, on a mandibular first molar.

	Pulp volume			
	Volume [mm³]	Mean [mm³]	SD [mm³]	Relative error [%]
1	29.1	28.9	0.45	0.9
2	28.2			-2.3
3	29.2			1.2
4	28.9			0.2

SD = standard deviation

Table 3A. Reproducibility of the mandible body height measurement.

	Body height			
	Volume [mm]	Mean [mm]	SD [mm]	Relative error [%]
1	29.2	28.9	0.51	1.2
2	28.2			-2.3
3	28.7			-0.5
4	29.3			1.6

SD = standard deviation

Table 4A. Tooth length measurements: tooth, crown and root length.

	Tooth length				Crown length				Root length			
Tooth number	**Ref mean[30] [mm]**	**Ref range[30] [mm]**	**Meas [mm]**	**Relative error [%]**	**Ref mean[30] [mm]**	**Ref range[30] [mm]**	**Meas [mm]**	**Relative error [%]**	**Ref mean[30] [mm]**	**Ref range[30] [mm]**	**Meas [mm]**	**Relative error [%]**
8	23.6	16.5–32.6	24.1	1.9	11.2	8.6–14.7	12.0	7.2	13.0	6.3–20.3	12.7	-2.5
9			24.2	2.7			11.7	4.3			13.2	1.4
7	22.5	17.7–28.9	20.5	-8.8	9.8	7.4–11.9	9.0	-7.8	13.4	9.6–19.4	12.0	-10.4
10			21.1	-6.2			9.5	-3.5			12.2	-9.2
6	26.3	20.0–38.4	24.0	-8.8	10.6	8.2–13.6	9.0	-14.7	16.5	10.8–28.5	15.4	-6.8
11			22.2	-15.6			9.4	-11.1			13.8	-16.4
5	21.5	15.5–28.9	19.4	-10.0	8.6	7.1–11.1	7.4	-13.5	13.4	8.3–19.0	12.9	-3.5
12			18.9	-12.1			7.3	-15.0			11.7	-12.4
4	21.1	15.2–28.4	19.8	-6.2	7.7	5.2–10.5	6.9	-10.6	14.0	8.0–20.6	13.7	-2.3
13			19.3	-8.3			6.9	-10.9			12.8	-8.7
3	20.1	17.0–27.4	17.5	-12.9	7.5	6.3–9.6	6.5	-13.6	12.9	8.5–18.8	11.6	-10.3
14			17.9	-10.9			7.1	-5.7			12.5	-3.1
2	20.0	16.0–26.2	18.9	-5.3	7.6	6.1–9.4	6.7	-12.1	12.9	9.0–18.2	12.6	-2.2
15			19.1	-4.6			6.7	-11.6			12.8	-1.1
1	17.5	14.0–22.5	14.6	-16.6	7.2	5.7–9.0	6.1	-15.0	10.8	7.1–15.5	9.65	-10.7
16			16.3	-7.0			6.3	-12.5			11.0	2.1
24	20.8	16.9-26.7	19.1	-8.0	8.8	6.3–11.6	8.4	-4.9	12.6	7.7–17.9	11.26	-10.6
25			19.3	-7.2			8.2	-6.5			11.81	-6.3
23	21.1	18.5–26.6	21.4	1.4	9.4	7.3–12.6	9.2	-2.3	13.5	9.4–18.1	12.88	-4.6
26			20.7	-2.0			8.8	-6.2			12.65	-6.3
22	25.9	16.1–34.5	22.4	-13.6	11	6.8–16.4	9.7	-11.7	15.9	9.5–22.2	13.65	-14.2
27			22.4	-13.4			10	-9.0			13.82	-13.1

21	22.4	17.0–28.5	22.3	-0.5	8.8	5.9–10.9	8.3	-6.2	14.4	9.7–20.2	14.57	1.2
28			21.9	-2.1			8.3	-6.0			14.25	-1.0
20	22.1	16.8–28.1	21.7	-1.6	8.2	6.7–10.2	7.9	-3.4	14.7	9.2–21.2	14.48	-1.5
29			21.4	-3.3			7.3	-10.9			14.66	-0.3
19	20.9	17.0–27.7	19.3	-7.7	7.7	6.1–9.6	6.4	-17.1	14.0	10.6–20.0	13.68	-2.3
30			19.3	-7.5			6.6	-13.9			13.28	-5.1
18	20.6	15.0–25.5	20.2	-2.1	7.7	6.1-9.8	7.0	-9.2	13.9	9.3–18.3	13.67	-1.7
31			19.9	-3.6			6.9	-9.9			13.6	-2.2
17	18.2	14.8–22.0	19.5	7.3	7.5	6.1–9.2	6.3	-16.5	11.8	7.3–14.6	14.13	19.7
32			18.5	1.7			6.5	-13.3			12.8	8.5

Ref = reference value; Meas = measured value; The tooth numbers, using the universal numbering system, are listed according to tooth type.

Table 5A. Tooth length measurements: mesiodistal and buccolingual diameter.

	Mesiodistal diameter				**Buccolingual diameter**			
Tooth number	**Ref mean[30] [mm]**	**Ref range[30] [mm]**	**Meas [mm]**	**Relative error [%]**	**Ref mean[30] [mm]**	**Ref range[30] [mm]**	**Meas [mm]**	**Relative error [%]**
8	8.6	7.1–10.5	9.0	5.1	7.1	6.0–8.5	7.5	5.3
9			9.2	6.7			7.3	3.3
7	6.6	5.0–9.0	6.6	0.7	6.2	5.3–7.3	6.2	-0.5
10			7.3	11.3			7.0	13.2
6	7.6	6.3–9.5	7.3	-4.3	8.1	6.7–10.7	7.8	-4.2
11			6.7	-11.6			7.9	-2.9
5	7.1	5.5–9.4	6.5	-8.4	9.2	6.6–11.2	9.3	1.5
12			7.0	-1.5			9.3	1.3
4	6.6	5.5–8.9	6.0	-9.3	9.0	6.9–11.6	9.1	1.6
13			5.9	-10.0			9.3	3.3

3	10.4	8.8–13.3	11.3	8.3	11.5	9.8–14.1	11.7	1.9
14			10.2	-2.1			11.0	-4.3
2	9.8	8.5–11.7	9.8	0.3	11.4	9.9–14.3	11.2	-1.7
15			10.0	1.6			11.2	-2.2
1	9.2	7.0–11.1	9.7	5.3	11.1	8.9–13.2	10.2	-7.7
16			9.2	0.5			10.1	-9.2
24	5.3	4.4–6.7	5.1	-4.5	5.7	4.8–6.8	5.1	-10.3
25			4.8	-9.0			5.3	-7.1
23	5.7	4.6–8.2	5.8	1.6	6.1	5.2–7.4	5.7	-6.7
26			5.9	3.0			6.1	-0.1
22	6.8	5.7–8.6	6.3	-6.8	7.7	6.4–9.5	7.0	-8.7
27			6.3	-6.9			7.0	-9.7
21	7.0	5.9–8.8	6.7	-4.6	7.7	6.2–10.5	8.0	3.9
28			6.5	-7.9			8.1	4.7
20	7.1	5.2–9.5	6.6	-6.6	8.2	7.0–10.5	8.7	6.1
29			7.2	1.9			8.4	3.0
19	11.4	9.8–14.5	11.4	-0.4	10.2	8.9–13.7	10.8	5.6
30			10.8	-5.7			10.6	3.6
18	10.8	9.6–13.0	11.0	2.0	9.9	7.6–11.8	10.8	9.2
31			10.8	0.1			10.1	1.9
17	11.3	8.5–14.2	10.7	-5.5	10.1	8.2–13.2	9.9	-1.5
32			11.3	-0.4			9.9	-1.7

Ref = reference value; Meas = measured value; The tooth numbers, using the universal numbering system, are listed according to tooth type.

Table 6A. Pulp volume measurements.

Tooth number	Ref mean[56] [mm³]	Ref SD[56] [mm³]	Ref min-max range[56] [mm³]	Meas [mm³]	Tooth number	Ref mean[56] [mm³]	Ref SD[56] [mm³]	Ref min-max range[56] [mm³]	Meas [mm³]
8	20.5	6.5	6.5 – 41.9	21.6	**24**	8.6	2.5	3.4 – 19.1	6.9
9				22.5	**25**				8.2
7	13.1	4.6	3.1 – 27.3	10.2	**23**	11.2	3.5	4.7 - 25.0	9.9
10				11.8	**26**				11.9
6	24.9	7.6	12.0 - 50.3	20.3	**22**	22.5	6.8	9.9 – 54.4	16
11				21.9	**27**				18.9
5	-	-	-	-	**21**	16.1	4.2	7.9 – 32.0	16.1
12				-	**28**				18.9
4	18.7	5.7	8.8 – 40.2	21.9	**20**	15.7	4.7	7.2 – 35.6	17.9
13				19.8	**29**				20.1
3	24.4	8.8	8.2 – 67.3	31.7	**19**	21.8	7.3	8.0 – 51.7	28.9
14				29.9	**30**				28.5
2	25.5	9.4	9.0 – 64.4	31.2	**18**	26.1	9.1	8.3 – 57.1	32.7
15				33.6	**31**				33.9
1	-	-	-	-	**17**	-	-	-	-
16				-	**32**				-

Ref = reference value; Meas = measured value; SD = standard deviation; min = minimum; max = maximum; The tooth numbers, using the universal numbering system, are listed according to tooth type.

Table 7A. Mandibular measurements.

Measurement type	Ref mean[31] [mm]	Ref SD[31] [mm]	Meas [mm]
Intergonial distance	86.0	4.9	84.0
Intercondylar distance	115.2	6.6	109.3
Body width	11.4	1.8	11.4
Pogonion-interdental distance	21.9	3.5	24.6
Body height	27.0	2.5	28.9
Body length	72.4	5.1	76.2

Ramus height	61.5	5.0	64.9
Pogonion-lateral condylar distance	114.3	4.5	117.3

Ref = reference value; Meas = measured value; SD = standard deviation